Moho and uppermost mantle structure in the Alpine area from

S-to-P converted waves

Rainer Kind[1,2], Stefan M. Schmid[3], Xiaohui Yuan[2], Benjamin Heit[2], Thomas Meier[4] and the AlpArray and AlpArray-SWATH-D Working Groups[5]

5   [1] Freie Universität Berlin, Berlin, Germany

[2] Deutsches GeoForschungsZentrum GFZ, 14473 Potsdam, Germany

[3] Eidgenössische Technische Hochschule Zürich, Switzerland

[4] Christian-Albrechts-Universität zu Kiel, Germany

[5] A full list of authors appears at the end of the paper

Correspondence to: Rainer Kind (kind@gfz-potsdam.de)

Abstract. In the frame of the AlpArray project we analyze teleseismic data from permanent and temporary stations of the Alpine region to study seismic discontinuities down to about 140 km depth. We average broadband teleseismic S waveform data to retrieve S-to-P converted signals from below the seismic stations. In order to avoid processing artefacts, no

15   deconvolution or filtering is applied and S arrival times are used as reference for stacking. We show a number of north-south and east-west profiles through the Alpine area. The Moho signals are always seen very clearly, and also negative velocity gradients below the Moho depth are visible in a number of profiles. A Moho depression is visible along larger parts of the Alpine chain. It reaches its largest depth of 60 km beneath the Tauern Window. The Moho depression ends however abruptly near about 13°E below the eastern Tauern Window. This Moho depression may represent the crustal trench, where the

20   Eurasian lithosphere is subducted below the Adriatic lithosphere. East of 13°E an important along-strike change occurs; the image of the Moho changes completely. No Moho deepening is found in this easterly region; instead the Moho is bending up along the contact between the European and the Adriatic lithosphere all the way to the Pannonian Basin. An important along strike change was also detected in the upper mantle structure at about 14°E. There, the lateral disappearance of a zone of negative velocity gradient in the uppermost mantle indicates that the S-dipping European slab laterally terminates east of the

25   Tauern Window in the axial zone of the Alps. The area east of about 13°E is known to have been affected by severe late-stage modifications of the structure of crust and uppermost mantle during the Miocene when the ALCAPA (Alpine, Carpathian, Pannonian) block was subject to E-directed lateral extrusion.

1 Introduction

The complicated tectonic structure of the Alpine mountain belt is a result of the collision of the African and European plates. A summary of tectonics, seismic investigations and still fundamentally open questions is given by a description of the recent AlpArray project by Hetényi et al. (2018a). One of the main goals of the AlpArray project is revealing the deep structure of the Eastern Alps. A comprehensive Moho map of the Alpine area has been published by Spada et al. (2013) combining controlled source seismics, receiver functions and local earthquake tomography. Earlier crustal models from controlled source studies have been published for example by Yan and Mechie (1989), Behm et al. (2007) and Grad et al. (2009a and b). Receiver functions have been used e.g. by Lombardi et al. (2008), Bianchi et al. (2015), Geissler et al. (2010) and Brückl et al. (2010), who published integrated models of the crust in the Eastern Alps. Most controlled source and receiver function data from the Eastern Alps indicate, like in the Central Alps, southward subduction of the European plate. In contrast, mantle tomography results in the Eastern Alps either indicates a change of subduction polarity by revealing a north-dipping slab or, alternatively, cannot resolve the polarity clearly (Lippitsch et al., 2003, Molinari et al., 2015; Guidarelli et al., 2017; Kästle et al., 2018, 2020). Also, the presence of both, an Eurasian southward dipping slab and an Adriatic northward dipping slab beneath the Eastern Alps have been proposed by Babuška et al. (1990) and only down to a depth of about 150 km by Kästle et al. (2020) and El-Sharkawy et al. (2020). A change of the subduction direction in the Eastern Alps is supported by geological arguments (Schmid et al., 2004; Kissling et al., 2006; Handy et al., 2015). In the last years large-scale international seismic experiments were carried out (CELEBRATION: see Hrubcová et al., 2005; AlpArray and EASI: see Hetényi et al., 2018a, b and SWATH-D: see Heit et al., 2017, 2021) and provided large amounts of new data. We used these new data from broadband stations together with data from earlier temporary experiments and from all available permanent broadband stations. We also processed the seismic records using a relatively novel method. This new method uses S-to-P conversions, similar to the S-receiver function method, except that raw untouched broadband data are stacked without any filtering or deconvolution. This method helps to avoid processing artefacts related to filtering (Kumar et al. 2010; Bodin and Romanowicz, 2014; Kind et al., 2020; Liu and Shearer, 2021). The S arrival times are automatically picked and used as reference. The differences to the S-receiver function method are that the waveforms are not modified by any filtering (including deconvolution) and that for stacking first arrival times of the SV signal are used and not the maxima of the modified SV waveforms.

2. Data and Method

All data used have been copied from the EIDA portals (e.g. http://www.orfeus-eu.org/data/eida). We selected events with magnitudes greater than 5.5 within the epicentral distances between 60° and 85°. Broadband data in time windows of 400 seconds before and after the theoretical S onset have been copied from the data archives. The distribution of stations used in the greater Alpine area is shown in Fig. 1. All networks contributing data are listed in the Acknowledgments. The basic idea was to stack nearly untouched common conversion point signals in the time domain with the arrival time of the SV signal as

60 reference. All other processing steps (like rotation of components, distance moveout correction, stacking or migration) are identical to the ones used in the receiver function technique. The three-component traces for each record are rotated from the Z, N, E coordinate system using the theoretical backazimuth and incidence angles according to the IASP91 model (Kennett and Engdahl, 1991) into the local ray coordinate system P, SV, SH (also called the L,Q,T system). We automatically picked the first arrivals of the SV signal (Baer & Kradolfer, 1987) using data with a signal-to-noise ratio

65 greater than 6 and corrected for the sign of the onset. The magnitude of the events was only considered for copying data from the archives. We normalized the traces with the absolute maximum within a window of 10 s after the S onset on the SV component. To ensure high-quality data we chose only events for which the amplitudes on the P component are less than 50 per cent of the input SV signal on the SV component within the time window of −50 to −10 s before the SV onset. The reason for applying this criterion is that very large signals on the P component within that window can only be regarded as

70 noise. At the same time, by lowering this limit too much we have significantly less data and may not be able to obtain a sufficient number of traces for summation. This is because the converted signals of interest are in most cases below the noise level in the individual traces. The expected S-to-P converted Moho signals are close to 10% of the incident signal and just a few percent in conversions from below the Moho. Signal generated noise is not expected before the SV signal. After applying these data quality criteria, more than 400,000 three-component records remained for analysis. To reduce the

75 amount of data we resampled all traces to 10 samples per second by linear interpolation. Before summation in time domain a distance moveout correction is applied in which we expanded or stretched the time scale to simulate a slowness of 6.4 s/° of the incoming wave. This is the slowness value frequently used in P and S-receiver function studies. S-to-P piercing point coordinates at depths of 50 and 100 km have been computed for the common piercing point (CCP) summation. The IASP91 model was used for these two processing steps. To process the data, we used the Seismic Handler software package

80 (Stammler, 1993; www.seismic-handler.org).

3. The Profiles

In order to obtain high resolution along the profiles we chose a size of the CCP area of 0.2° in a direction parallel to the profiles. However, to keep the CCP area large enough for a sufficient number of traces used for the summation, we increased the extension of the CCP area perpendicular to the profile up to 1.0° or more. Profiles with a smaller extension of the CCP

85 area perpendicular to the profile are shown in the Supplementary Material for comparison. The locations of the chosen profiles are displayed in Fig. 2 and the corresponding seismic sections are shown in Figs. 3-14. The panels on the left side of the figures (labeled A) are for piercing points at 50 km and the panels on the right side (labeled B) are for piercing points at 100 km depth. This means that the summation traces are best focused at these particular depths. The traces in the same geographical bins between A and B are not identical. Consequently, the left-hand panels focus on the Moho depth while the

90 right-hand panels point at discontinuities below the Moho. Each trace results from summing of at least 200 traces. The precursor time is given on the left scale relative to the SV arrival time. A depth scale is given on the right side of each figure.

These depths were computed using the one-dimensional IASP91 global reference model. We provided the time scale in order to enable the use of alternative models for depth calculation. The amplitude scale is given relative to the amplitude of the incident SV signal. The latitude or longitude of the center of each bin is given at the top of each figure. There is no overlapping between neighboring traces along the profiles. The width of the profiles is given at the bottom of each figure.

The signals converted from S to P at the Moho are blue and denote an increase of velocity with increasing depth. Red signals denote a downward velocity decrease. The arrival times of the seismic signals must be picked as usual in seismograms at the beginning of the signals and not at the signal maximum, as is usually the case for the classical receiver function method. Picking arrival times of weak emergent signals like converted waves from the Moho or deeper discontinuities is frequently a difficult problem, which we are still trying to improve. Therefore we marked so far by visual inspection only approximate Moho arrival times with dotted lines. A more accurate way to determine Moho arrival times would be a waveform correlation with the SV signal form, which we plan in future. The signal forms of the Moho (and other) conversions are determined mainly by the signal forms of the incident SV signals. The response of the structure below the station (mainly the Moho interface) is also contributing to the signal form. Below the Moho in the right-hand panels we see, for most of the profiles, concentrations of red signals. These are caused by sharp or gradual downward velocity decreases. These signals below the Moho appear scattered, and lack clear lateral correlations, when compared to the Moho signals, that align much better. For this reason, we refer to the red regions below the Moho as zones of Negative Velocity Gradients (NVG). In some profiles we marked the bottom of a significant NVG group by a broad grey line that approximately indicates the arrival times of a group of scatterers. A negative seismic velocity gradient is often expected to mark the lithosphere asthenosphere boundary. But its depth depends on the nature of the geophysical measurements used to locate this boundary. Apart from temperature effects this negative gradient may also be caused by changes in, for example, chemical composition or anisotropy (e.g. Eaton et al., 2009). Therefore, we prefer to use the neutral term NVG here.

4. Characteristic Observations Along the Profiles

4.1. Moho Structure

4.1.1. North-south profiles

We first present a series of north-south oriented profiles shown in Figs. 3-9. In the entire region between 8.0 to 13.5°E (profiles 2-6 in Figs. 4A-8A) we see a south dipping European Moho marked by black dotted lines. The Moho reaches its largest depth in all profiles 2-6 at about 46.5° N. This is near the latitude at which Spada et al. (2013) draw the boundary between European and Adriatic Moho, respectively (see black line in Fig. 2) that roughly coincides with the location of the E-W striking part of the Periadriatic line west of longitude 13°E. This implies that, according to geological evidence (Schmid et al. 2004; Kissling et al. 2006), the Moho south of about 46.5° N, depicted in the profiles 2-6, is the Adriatic Moho. In

profiles 2-6 this Adriatic Moho rises towards a possible culmination located near 45.5°N before descending southward beneath the Ligurian Moho at the front of the Apennines. This is shown by the onsets of the Adriatic Moho, which is also

125   marked by dotted black lines (Figs. 4A-8A). At first sight, this geometry suggests a wedge-shaped trough below the Alpine chain. In fact, the two Moho's are separated from each other by a subduction corridor, whereby the European Moho dips undisputedly southward beneath the Adriatic Moho according to geological and geophysical evidence (Schmid et al. 2004; Kissling et al. 2006), west of 11°E. A far-reaching European Moho below the Adriatic Moho is, however, not observed in our data. This is different to the continental collision observed between India and Asia in Tibet where a double Moho is

130   observed and is interpreted as Indian lower crust reaching several hundred kilometers below the Tibetan crust (e.g. Yuan et al. 1997, Nabelek et al. 2009). In the Alps, east of 11°E opinions about the subduction polarity have remained controversial so far (see discussion in Kästle et al. 2020). The maximum depth of the Moho reaches about 50 km near 8.5°E (Fig. 4A) and increases to about 60 km near 13°E (Fig. 8A). A very similar maximum Moho depth is also observed in the west near 7.5°E. Here the Moho depth reaches about 65 km at about 45.5°N (see profile 1 Fig. 3A). This Moho interface is hence located

135   further south, which is caused by the south bending of the Alpine chain in the west (Fig. 2).
A significant change in the structure of the Moho below the Alps is observed near 13° E, i.e. near the eastern margin of the Tauern Window by comparing the Fig. 8A with Fig. 9A. West of this longitude the maximum depth of the Moho depression is around 60 km at 47°N (white arrow in profile 6 of Fig. 8A). East of 13.5°E the Moho depth at 47°N is only about 40 km (white arrow in profile 7 of Fig. 9A), and the Moho depression near latitude 47° seen in Fig. 8A is suddenly replaced by a

140   culmination at the same latitude. This implies that the Moho topography no longer reflects a depression that would be expected to coincide with a scenario of subduction of the European plate below the Adriatic plate (or the opposite) in the Alps east of about 13°E.

On the other hand, a so far unknown substantial Moho depression similar to that observed at the plate interface west of 13°E

145   is observed further in the north (at 48-49°N) in the profiles east of about 13°E (see profiles 7-9 in Figs. 9A-11A). In the case of the profiles 7 and 8 this Moho depression is located north of the Alpine front (marked with red arrows in Figs. 9A and 10A; see also Fig. 2) and beneath the southern Bohemian Massif belonging to the European plate.

In the very wide (between 17-19°E) profile 9 (Fig. 11A) the Moho is observed to culminate in the area of the Pannonian

150   Basin, combined with a jump in the Moho onset time is seen near 47°N marked with a black arrow. This occurs at the location of the Mid-Hungarian Fault Zone (MHZ in Fig. 2, e.g. Hetényi et al. 2015). North of this fault zone the Moho is at about 30 km and deepens to 50 km underneath the frontal West Carpathians. South of the MHZ the Moho rises to about 25 km depth beneath the part of the Pannonian Basin located south of Lake Balaton. Moho depths of around 50 km have not been observed at the southern edge of the Bohemian Massif before. Hrubcová et al. (2005) and Wilde-Piórko et al.

155   (2005) located the Moho in this region near 40 km depth based on seismic refraction data and receiver functions. Hetényi et al. (2015) observed a Moho depth of 25-30 km across the MHZ using P-receiver functions. Horváth et al. (2015) had

obtained similar Moho depths from refraction lines. Szanyi et al. (2021) did not observe Moho signals in an ambient noise tomography study. The reason for such discrepancies regarding the Moho depths at the southern edge of the Bohemian Massif and around the MHZ could be as follows. If we look at the maxima of the Moho signals across the MHZ (marked

160 approximately by the red dotted line in Fig. 11A), no significant jump is visible across the MHZ. We also note that the signal form of the Moho conversion is shorter south of the MHZ than north of it. Therefore, the earlier Moho onsets north of the MHZ might be explained by precursors of the actual Moho signal due to the existence of a second discontinuity located below the actual Moho north of the MHZ. The onset of the actual Moho could, in this case, not be adequately identified anymore. This phenomenon could also mean, that the first arrivals identified as Moho at the boundary of the Bohemian

165 Massif could originate from a discontinuity below the Moho. Of course, variation in the average crustal velocity change the Moho onset time. However, since the main part of the Moho signal remains unchanged across the MHZ, it seems likely that the average crustal velocity is also relatively unchanged.

We think that a better way to determine Moho onset times would be the comparison of the SV signal form with the Moho signal form, which we plan for a later time. In the Supplementary Materials (Figs. S9-S11) we present higher resolution

170 profiles across the MHZ, which, however, have a lower signal-to-noise ratio due to fewer traces in the stacking area. The influence of potentially different velocity models is not considered in the Moho depth estimates discussed above. Fig. 15 summarizes locations and maximum depths of the Moho along the Alpine chain in map view.

4.1.2. East-west profiles

In a second step we discuss the Moho depth shown along three east-west profiles presented in Figs. 12A-14A. Fig. 12A

175 shows profile 10 centered at 47°N and entirely located on the European plate east of longitude 11.5°E but straddling along the plate boundary with Adria further to the east. This profile reaches the maximum Moho depth of around 60 km at about 13°E, i.e. in the area of the Tauern Window (see Fig. 2). Eastward, the Moho depth of this profile steadily rises to less than 20 km beneath the Pannonian Basin. West of its deepest point beneath the Tauern Window the Moho also rises, but exhibits a secondary depression between 7-8°E located in the European plate near the Alpine Front (Fig. 2). For easier comparison

180 the dotted black line marking the Moho trend in Fig. 12A is copied into the neighboring profiles 11 and 12 located north and south of profile 10, respectively (Figs. 13A and 14A). Profile 11 (Fig. 13A) located further north at 48°N, entirely runs within the European plate and is similar to the one at 47°N (Fig. 12A). However, in its western part the Moho is generally shallower in profile 11, probably due to the proximity to the Rhine Graben. Conversely, in the eastern part of this profile 11 the Moho is generally deeper than that of profile 10 at 47°N. This confirms the existence of a substantial Moho depression

185 beneath the Bohemian Massif, which was found in the N-S profiles 7 and 8 (Figs. 9A and 10A). This profile 11 (Fig. 13A) also shows that the shallowing of the Moho towards the east is by far more moderate compared to that seen in profile 10. The southernmost E-W profile 12 at 46°N (Fig. 14A) runs within the Adriatic plate east of longitude 8.5° and shows a Moho trend that is very similar to the one at 47°N (Fig. 12A). Only in its western part, running within the European part, the Moho is somewhat deeper.

4.2. Structure within the uppermost Mantle

The left and right panels of Figs. 3-14 show profiles of summed traces, which have their piercing points within the same geographical bins. However, the piercing points are computed for different depths, namely 50 km for the left hand panels and 100 km for the right hand panels. Therefore, the summed traces in the bins are not identical. We now focus on the right panels computed by choosing a piercing point of 100 km, which is optimal when searching for structures in the shallow mantle below the Moho. Almost all Figs. 3B-14B show a relatively large number of negative signals (marked in red) indicating downward velocity reductions at some depth below the Moho. However, there are significant differences between these red signals compared to the blue signals marking the Moho. The amplitude of the Moho signals is nearly 10% of the incident SV wave, whereas the amplitude of the negative signals from below the Moho is in most cases below 4%. Moreover, in most cases the Moho signals mark a clear discontinuity, which can be correlated over the entire length of the profiles, whereas the negative signals from below the Moho do not mark a clear discontinuity but appear much more scattered. However, in parts of some of the profiles we were able mark the lower boundary of regions with exceptionally high concentrations of negative signals with a scattered grey line. We refer to such red regions as Negative Velocity Gradient zones (NVG). The broad grey lines approximate the onset times of the scatterer group in this time window.

4.2.1. North-south profiles

An NVG could be mapped in profile 1 (Fig. 3B), south dipping down to about 110 km. In profiles 2-4 (Fig. 4B-6B, between 8-11°E) the NVG is horizontal or slightly inclined to the south. The base of the NVGs is found at depths of 80-90 km, and they end towards the south at around latitude 47° to 48°, i.e. at or near the front of the Alps (see Fig. 2). This shows that they are definitely embedded in the European plate of the Alpine foreland dipping southwards underneath the front of the Alps. In profiles 5-7 (Figs. 7B-9B, between 11-14.5°E), the NVGs appear more pronounced. They are again south dipping and their base reaches down to 115-130 km depth. They also end southward at around latitude 47°, which is somewhat further inside the Alps given the SSW-ENE strike of the Alpine front but still within the European plate (see Fig. 1). However, there is practically no significant indication of an NVG in profile 8 (Fig. 10B, 14.5-17°E), i.e. in the area located well east of the Tauern Window spanning the Alps-Carpathians transition area (see Fig. 1). Note that profile 8, together with profile 9, was chosen relatively wide because of the scarcity of stations in the area. In the easternmost N-S profile 9 east of 17°E (Fig. 11B) running across the Western Carpathians and across the MHZ, a very different structure of the NVG is seen. The NVG is subhorizontal north of about 48.5°N, where the base of the NVG shows a significant step moving up from 90 km beneath the European foreland and the external Carpathians to 60 km beneath the internal Carpathians and the Pannonian plain. We note that this jump in the depth of the NVG closely coincides with the onset of massive thinning of the lithosphere in the wider Pannonian realm that also affects the Central Western Carpathians south of about 48.5° (see Fig. 10 of Horváth et al. 2006).

 4.2.2. East-west profiles

The east-west profile 10 centered along 47°N (Fig. 12B) shows a very clear NVG that steeply dips eastward and reaches about 130 km depth at 13°E where it turns horizontal and disappears near 14E. Comparing this easterly dip of the NVG in an E-W profile with its southerly dip in the N-S profiles at 11°-14.5°E (Figs. 7-9) shows that the NVG is in fact dipping towards the southeast. The east-west profile 11 along 48°N (Fig. 13B) along the northern Alpine front also shows an apparently east dipping NVG, however only reaching about 110 km depth at around 12°E. Profile 12 along 46°N (Fig. 14B) below the Po valley and located within the Adria plate in its eastern part, however, lacks a similar east dipping NVG. It seems astonishing that relatively steeply dipping structures can be imaged by steeply incident converted waves. Our interpretation is that the NVG area may contain a sufficient number of horizontal scatterers, which can be observed. The dip angle of the NVG might be biased (Schneider et al., 2013). Fig. 16 summarizes the deepest locations of the bottom of the NVG in the Spada (2013) Moho map and shows that they are all located in the area of the European plate. These deepest points are located (1) in the northern Alpine foreland (Bohemian Massif), (2) in the frontal part of the West Carpathians and (3) beneath the axial zone of the central and Eastern Alps, where they reach depths between 110 km and 130 in an area close to the southern margin of the European plate and in the vicinity of its contact with the Adria plate.

5. Comparison with Earlier Results

The comparisons of our results with those obtained by previous studies are discussed here and are displayed in Figs. 17 to 20.

In Fig. 17A we compare our Moho data obtained along the north south profile 6 centered at 13°E (Fig. 8) with the results of Hetényi et al. (2018b) and Bianchi et al. (2020) along their profile at 13.3°E (temporary passive experiment EASI). Hetényi et al. (2018b) used P-receiver function data from this profile between the Eger Rift in the northern part of the Bohemian Massif and the Adriatic Sea. Their recorded Moho depth is plotted as cyan dotted line along our section 6 in Fig. 17A. Their Moho depth increases from 25 km at the Eger Rift at the northern end to about 30 km at the Alpine front at 48°N. From there the European Moho deepens rapidly to about 60 km at 47°N below the Tauern Window. The northward dipping Adriatic Moho reaches deeper down to 70 km and dips below the European Moho according to these authors. This is not seen in our results. The very general shape of the Moho is nevertheless in good agreement with our data. However, their depths of the European and Adriatic Moho are about 5 km shallower than ours, except near the deepest point at 47°N. This might partly be due to the different velocity models used. Hetényi et al. (2018b) used a local model whereas we used a global model (IASP91). Our data do not support the postulate of Hetényi et al. (2018b) that the Adriatic Moho in the Eastern Alps dips northward underneath the European Moho. Instead, our Moho depression looks rather symmetric similar to Spada et al. (2013). Bianchi et al. (2020) used PKP multiples within the crust below the seismic stations to derive the Moho depth. Their results are marked by a slight grey dotted line in Fig. 17A. The agreement between our data with those of Bianchi et al.

(2020) is also reasonably good, except near 47°N, where they have no data. It should also be noted, that the "Moho gap" mapped in white by Spada et al. (2013) at 47°N (Fig. 2) does not seem to exist according to our data, and similar to those of Mroczek et al. (2020) and Hetényi et al. (2018b).

255

In Fig. 17B, depicting the E-W profile 10, we compare our data regarding the NVG in the upper mantle below the Moho (previously discussed and illustrated in Fig. 12B) with results from the teleseismic body wave tomography by Paffrath et al. (2021) by superimposing the P-wave velocity contours that these authors used for calculating velocity anomalies along the

260 same E-W profile 10. There is fairly good agreement between the two data sets in the western part of the profile between longitudes 5° and 12°. In this area the E-dipping base of the red NVG zone roughly coincides with the top of an area associ-ated with abnormally low P-wave velocities below 8.0 km sec^{-1} marked in yellow in the western part of the profile. This same NVG zone was also traversed by the N-S profiles of sections 4 to 7 (Figs. 6-9) that show the NVG zone to be hosted within the SE-dipping European plate. However, while the data of Paffrath indicate a major change to occur already east of

265 longitude 12°E where the mantle tomography indicates eastward shallowing of the top of the zone of low P-wave anomalies, our NVG zone hosted in the European lithosphere can be followed until longitude 12°E (green line in Fig. 12B), terminating at around 15°E. Hence, the agreement between the two methods is poor between 12°E and 14°E. Further studies and high-resolution S-wave velocity models are needed to resolve this discrepancy. In this context it should, however, be noted that our method of using converted waves is sensitive to velocity gradients and not absolute velocities. This means that smaller

270 scale relative velocity reductions could well be embedded in larger high or low velocity regions. Further studies and high-resolution S-wave velocity models are needed to resolve this discrepancy. In spite of the discrepancies between the two data sets in the 12-14°E sector the data of Paffrath et al. (2021) confirm that a first order lateral change to occurs in the area of the Tauern window. East of this area the SE-dip of the European lithosphere laterally terminates, giving way to a different sce-nario that indicates eastward shallowing of the Moho (our data) that coincides with the lateral disappearance of the NVG

275 (see yellow area marking velocities <8.0 km sec-1 in Fig. 17B) according to the velocities provided by the model of Paffrath et al. (2020).

Geissler et al. (2010) presented a map of (what was called) the lithosphere-asthenosphere boundary (LAB) of central Europe obtained from an S-receiver function study (their Fig. 9). We compare their LAB observations with our NVG observations in

280 the eastern Alps. They used the classical S-receiver function method with deconvolution before stacking, whereas we use stacking of the original untouched broadband data. Our east-west profile 10 (Fig.12) between 46.5 and 47.5°N covers approximately the profiles I and J (Fig.9, Geissler et al. 2010). We see in profile 10 between about 12 and 15°E a steeply east dipping NVG reaching from about 90 to 140 km depth. They observe in the approximately the same area an east dipping LAB from about 100 to 150 km depth. This can be considered a very good agreement taking into account the different

285 stacking areas used in both studies. Geissler et al. (2010) used a 1°x 1° area. We used a stacking area of 1° latitude and 0.2°

longitude, since we had more date available, which resulted in higher resolution. We note that the area where we observe this steeply east dipping NVG, which confirms similar observations by Geissler et al. (2010), is practically the same area where Lippitsch et al. (2003) observe a north-east dipping slab in a tomography study.

290   Fig. 18A compares our north-south Moho profile 6 with the Eastern Alps Moho profile by Behm et al. (2007) and Brückl et al. (2010) at 13°E. The agreement of the profiles is very good. The general conclusion of Brückl et al. (2010) that the European Moho is subducting below the Adriatic Moho is not obvious from our data, but the asymmetry in our data is in favor of this conclusion. Our data compare fairly well with the data of Kummerow et al. (2004) along their profile at 12°E (which is about 80 km further west) although their Moho depths appear shallower. In Fig. 18B we compare our north-south

295   profile along a corridor between 10 and 12°E with a profile in the map of Spada et al. (2013) (see Fig. 2) at 11°E. The agreement between the two data sets is good. North of 47°N our Moho seems to be in average about 5 km deeper. The reason is not exactly known. This might be caused by differences in the background models used for the time-depth migration. The Moho jump near 44°N marking the transition from the Adriatic to the Ligurian Moho is evident on both profiles.

300

In Fig. 19A we compare our Moho data along profile 9 (Fig. 11A) depicting a culmination of the Moho with the RF data of Hetényi et al. (2015) by projecting the northwest-southeast profile of Hetényi et al. (2015) onto our north-south profile. This same Moho culmination follows the strike of the MHZ and was traced further to the ENE by Kalmár et al. (2019). North of the MHZ the Moho is rapidly deepening towards the north. Fig. 19B compares our profile 9 (Fig. 11B) with mantle

305   tomographic results from Paffrath et al. (2021), geologically interpreted by Handy et al. (2021). The NVG in Fig. 19B to both sides of the MHZ, which is very shallow and located immediately below the Moho, is not changing depth across the MHZ at 47°N where the Moho starts to deepen (see Fig. 19A). Rather, an offset of the NVG to greater depth occurs at around 48.5N, which is located within the Central West Carpathians, i.e. north of the Pannonian Basin. The comparison with the tomographic data shows that this jump in depth of the NVG coincides with the location of the Alpine-Tethys suture zone

310   identified in tomography data (Handy et al. 2021), a zone that forms the southern boundary of the European lithosphere (green dotted subvertical line in Fig. 19B). Our data reinforce the fundamental difference between the seismic properties of the European lithosphere beneath the frontal Western Carpathians with those of the more internal parts of the Western Carpathians and the Pannonian realm characterized by a shallow lithosphere-asthenosphere boundary (e.g. Horváth et al. 2006; Kind et al., 2017).

315

In Fig. 20A we compare our Moho depth profile along the east west profile 10 at 47°N (Fig. 12A) with early results of seismic refraction experiments (Yan and Mechie, 1989). The agreement in the general trend of eastward shallowing starting in western Tauern Window at around 12°E is good. Fig. 20B presents an additional profile 13 located north of profile 11 at 49-50°N in the European lithosphere crossing the front of the Western Carpathians at 17.5°E (Fig. 2), added for comparison

320 with the Moho map of Grad et al. (2009a), based on a variety of geophysical data. The cyan dotted line in this Fig. 20B marks the rapid eastward Moho deepening towards the front of the Western Carpathians initiating at ca. 14°E and reaching 50 km below the external Western Carpathians. The discrepancy with the data of Grad et al. (2009a) is considerable in the easternmost part of this profile where our data show a much more pronounced deepening of the Moho. This eastward deepening along the northerly profile of Fig. 20B strongly contrasts with the eastward shallowing of the Moho shown in Fig.

325 20A, i.e. in a more southerly profile (at 46.5-47.5°N) crossing the area of the northern margin of the Pannonian plain around the MHZ. This marked difference is due to the fact that in our data the Moho in the profile of Fig. 20B located in the European lithosphere which bends down across the SW-NE striking front of the Western Carpathians (see Fig. 2) while the profile of Fig. 20A runs within the Pannonian realm characterized by the eastward shallowing Moho depth shown in E-W profiles 10, 11 and 12, caused by Miocene backarc extension in the Pannonian Basin, along the MHZ and in the internal

330 parts of the Western Carpathians region (Horváth et al., 2015).

6. Summary of Observational Results

The comparison with results from other studies using other methods shows that by using broadband S-to-P converted signals we are able to obtain clear images of the Moho topography along most of the Alpine chain and also reveal the presence of some features that were not detected before. Furthermore, this method allows highlighting an important along-strike change

335 regarding Moho topography that takes place at around 13°E, i.e. in the eastern Tauern Window. The Moho-depression beneath the Central Alps along the Europe-Adria lithosphere boundary along 47°N deepens from some 50 km at 8°E to 60 km at around 13°E. In the N-S profiles the Moho depression very abruptly makes place to an up-doming of the Moho along the axial zone of the Alpine orogen at around 13°E, persisting all the way into the Pannonian Basin, as the depth of the Moho generally decreases to < 30 km also N and S of 47°N. Our data also indicate the existence of a substantial Moho depression

340 east of 13°E and near the Alpine frontal thrust extending eastward into the area of the frontal Western Carpathians whose extent remained so far undetected (see Fig. 15).

In the shallow mantle we also observe, extending from 10°E to14°E, along an E-W section along 47°N combined with N-S sections, steeply SE-dipping areas of downward velocity reductions referred to as NVGs that extend to at least 140 km depth

345 at 14°E and disappear east of there. The base of the NVG, which roughly coincides with the top of a low velocity zone revealed by mantle tomography west of 12°E (Paffrath et al. 2021) is related to the European slab. The termination of the NVG at 14°E suggests an important along strike change also in terms of the shallow mantle structure taking place at 14°E, i.e. about 1° east of the along strike change observed for the Moho-topography. Below the frontal West Carpathians at about 49°N we observed a jump of the base of the subhorizontal NVG from about 60 km in the south to 90 km in the north.

7. Discussion and Conclusions

From a technical point of view the improved images of the present paper are, besides the obvious reason of using much larger amounts of data, also due to the modified data processing technique. In the receiver function technique seismic traces are sometimes filtered without paying sufficient attention to sidelobes or acausality. Another problem is the waveform compression caused by deconvolution and summation along the maximum of the compressed signals, which also produces sidelobes that tend to be misinterpreted. We therefore avoided all filtering and lined up the traces along the onsets of the S signals for summation. We found good agreements of our results with earlier results obtained in many regions. This emphasizes the reliability of our results. We also think that using additional seismic phases could help to increase the reliability of the seismic images and in consequence of the tectonic interpretation. A good example is the usage of PKP multiples below the stations as shown by Bianchi et al. (2020).

From the geological point of view the Moho topography reflects deeper subduction of the European lithosphere only west of and in the Tauern Window area. This is no more the case east of 13° E, i.e. east of the eastern Tauern Window, where the Moho is up domed in the contact area between the European and the Adriatic lithosphere. According to geological evidence (Ratschbacher et al. 1991) and according to the geological interpretation of recent mantle tomographic data (Paffrath et al. 2021, Handy et al., 2021) this updoming is likely due to a late stage modification of the Moho topography in the Eastern Alps, the Western Carpathians and the Pannonian Basin that occurred during the last ca. 20 Ma. Such updoming goes together with crustal thinning associated with lateral extrusion of the so-called ALCAPA mega-unit associated with the N-directed indentation of the Dolomites indenter and roll back of the Eastern Carpathians (Ratschbacher et al. 1991). The rapid jump of the base of the NVG from about 60 km in the south to 90 km in the north below the frontal West Carpathians at about 49°N is also related to extension and asthenosphere upwelling in the Pannonian Basin that also affected the internal Western Carpathians (Horváth et al. (2015).

Three main additional salient new features are of importance: (1) The possible existence of a second discontinuity below the Moho north of the Mid-Hungarian Fault Zone emphasizes the important role this fault zone played in terms of lateral offsets that occurred during the lateral extrusion of ALCAPA during the Miocene (Schmid et al. 2008), and, (2) A second Moho trough was detected north of the Alps, reaching down to about 50 km depth and located in the Bohemian Massif north of the Alpine front in the Eastern Alps, extending eastward into the frontal part of the Western Carpathians. This structure, hosted in the European lithosphere, has not been observed before and cannot be interpreted yet at this stage. Further studies are needed to clarify this structure. (3) We observed areas of downward velocity reductions referred to as NVGs hosted within the European lithosphere in the foreland of the Alps at a depth of 80-90 km. In the Eastern Alps west of 14°E these NVGs can be traced down to depths of 115-140 km all the way to latitude 47°N, i.e. into the axial zone of the Alps (marked NVG in Figs. 9B and 12B).

Team list. Members of the AlpArray Seismic Network and AlpArray-SWATH-D Working Groups: György HETÉNYI, Rafael ABREU, Ivo ALLEGRETTI, Maria-Theresia APOLONER, Coralie AUBERT, Simon BESANÇON, Maxime BÈS DE BERC, Götz BOKELMANN, Didier BRUNEL, Marco CAPELLO, Martina ČARMAN, Adriano CAVALIERE, Jérôme CHÈZE, Claudio CHIARABBA, John CLINTON, Glenn COUGOULAT, Wayne C. CRAWFORD, Luigia CRISTIANO, Tibor CZIFRA, Ezio D'ALEMA, Stefania DANESI, Romuald DANIEL, Anke DANNOWSKI, Iva DASOVIĆ, Anne DESCHAMPS, Jean-Xavier DESSA, Cécile DOUBRE, Sven EGDORF, ETHZ-SED Electronics Lab, Tomislav FIKET, Kasper FISCHER, Wolfgang FRIEDERICH, Florian FUCHS, Sigward FUNKE, Domenico GIARDINI, Aladino GOVONI, Zoltán GRÁCZER, Gidera GRÖSCHL, Stefan HEIMERS, Ben HEIT, Davorka HERAK, Marijan HERAK, Johann HUBER, Dejan JARIĆ, Petr JEDLIČKA, Yan JIA, Hélène JUND, Edi KISSLING, Stefan KLINGEN, Bernhard KLOTZ, Petr KOLÍNSKÝ, Heidrun KOPP, Michael KORN, Josef KOTEK, Lothar KÜHNE, Krešo KUK, Dietrich LANGE, Jürgen LOOS, Sara LOVATI, Deny MALENGROS, Lucia MARGHERITI, Christophe MARON, Xavier MARTIN, Marco MASSA, Francesco MAZZARINI, Thomas MEIER, Laurent MÉTRAL, Irene MOLINARI, Milena MORETTI, Anna NARDI, Jurij PAHOR, Anne PAUL, Catherine PÉQUEGNAT, Daniel PETERSEN, Damiano PESARESI, Davide PICCININI, Claudia PIROMALLO, Thomas PLENEFISCH, Jaroslava PLOMEROVÁ, Silvia PONDRELLI, Snježan PREVOLNIK, Roman RACINE, Marc RÉGNIER, Miriam REISS, Joachim RITTER, Georg RÜMPKER, Simone SALIMBENI, Marco SANTULIN, Werner SCHERER, Sven SCHIPPKUS, Detlef SCHULTE-KORTNACK, Vesna ŠIPKA, Stefano SOLARINO, Daniele SPALLAROSSA, Kathrin SPIEKER, Josip STIPČEVIĆ, Angelo STROLLO, Bálint SÜLE, Gyöngyvér SZANYI, Eszter SZŰCS, Christine THOMAS, Martin THORWART, Frederik TILMANN, Stefan UEDING, Massimiliano VALLOCCHIA, Luděk VECSEY, René VOIGT, Joachim WASSERMANN, Zoltán WÉBER, Christian WEIDLE, Viktor WESZTERGOM, Gauthier WEYLAND, Stefan WIEMER, Felix WOLF, David WOLYNIEC, Thomas ZIEKE, Mladen ŽIVČIĆ, Helena ŽLEBČÍKOVÁ

Author contributions. Rainer Kind developed the initial idea of the project. Rainer Kind and Xiaohui Yuan did the data processing. Stefan Schmid and Thomas Meier did most of the interpretation and Ben Heit installed the stations in cooperation with the SWATH-D working group and participated in the interpretation

Competing interests. The authors declare that they have no conflict of interest.

Acknowledgments

This research was carried out within the AlpArray and SWATH-D projects which have been funded by the Deutsche Forschungsgemeinschaft within the Priority Program "Mountain Building Processes in Four Dimensions (MB-4D)" and by the GeoForschungsZentrum Potsdam. We are deeply indebted to all people involved in the instrument preparation, fieldwork

415 and data archiving. We thank numerous landowners for their willingness to host the stations, and all communities, authorities and institutes in the region for their great support of the project. Data of the SWATH-D network are archived and available from the GEOFON data center (Heit et al., 2017, 2021). AlpArray backbone data are archived at EIDA (http://www.orfeus-eu.org/data/eida). Instruments for the SWATH-D network were provided by the Geophysical Instrument Pool Potsdam GIPP of the GFZ Potsdam. Discussions with many colleagues within the Priority Program are greatly acknowledged. The tectonic
420 map was compiled by M.R. Handy. We also wish to thank Emanuel Kästle for his support. Most of the plotting has been done with GMT. We also thank two anonymous reviewers for their very constructive comments.

The following networks have contributed data to this study:

PASSEQ (7E), Albanian Seismological Network (AC), Belgian Seismic Network (BE), Bayernnetz (BW), Switzerland Seismological Network (CH), Croatian Seismograph Network (CR), Czech Regional Seismic Network (CZ), Danish
425 Seismological Network (DK), Estonian Seismic Network (EE), Northern Finland Seismological Network (FN), RESIF and other broadband and accelerometric permanent networks in metropolitan France (FR), GEOFON (GE), German Regional Seismic Network (GR), Regional Seismic Network of North Western Italy (GU), Finish National Seismic Network (HE), Hungarian National Seismological Network (HU), Global Seismograph Network - IRIS/USGS (IU), Italian National Seismic Network (IV), Mediterranean Very Broadband Seismographic Network (MN), Netherlands Seismic and Acoustic Network
430 (NL), Austrian Seismic Network (OE), North-East Italy Seismic Network (OX), Polish Seismological Network (PL), CEA/DASE Seismic Network (RD), Romanian Seismic Network (RO), Province Südtirol (SI), Serbian Seismological Network (SJ), Slovak National Seismic Network (SK), Seismic Network of the Republic of Slovenia (SL), Trentino Seismic Network (ST), SXNET Saxon Seismic Network (SX), Thüringer Seismologisches Netz (TH), Eifel Plume (XE), EASI Eastern Alpine Seismic Investigations (XT), Alparray (Z3), TOR-TE (ZA), SVEKALAPKO (ZB), TOR-TO (ZC), Transalp
435 II (ZO), SWATH-D (ZS), Bohema (ZV), JULS (ZW).

References

Babuška, V., Plomerová, J., and Granet, M.: The deep lithosphere in the Alps: a model inferred from P residuals, Tectonophysics 176, 137-165, 1990.
Baer, M., and Kradolfer, U.: An automatic phase picker for local and teleseismic events, Bull. Seism. Soc. Am., 77(4),
440 1437–1445, 1987.
Behm, M., Brückl, E., Chwatal, W., and Thybo, H.: Application of stacking and inversion techniques to three-dimensional wide-angle reflection and refraction seismic data of the Eastern Alps. Geophys. J. Int. 170, 275–298, https://doi.org/10.1111/j.1365- 246X.2007.03393.x, 2007.
Bianchi, I., Behm, M., Rumpfhuber, E. M., and Bokelmann, G.: A new seismic data set on the depth of the Moho in the
445 Alps. Pure Appl. Geophys. 172, 295–308, doi: 10.1007/s00024-014-0953-1, 2015.

Bianchi, I., Ruigrok, E., Obermann, A., and Kissling, E.: Moho topography beneath the eastern European Alps by global phase seismic interferometry, Solid Earth, https://doi.org/10.5194/se-2020-179, 2020.

Bodin, T., Yuan, H. and, Romanowicz, B.: Inversion of receiver functions without deconvolution-application to the Indian craton, Geophys. J. Int. 196 (2), 1025-1033, https://doi.org/10.1093/gji/ggt431, 2014.

450   Brückl, E., Behm, M., Decker, K., Grad, M., Guterch, A., Keller, G.R., and Thybo, H.: Crustal structure and active tectonics in the Eastern Alps, Tectonics, 29, TC2011, doi:10.1029/2009TC002491, 2010.

Eaton, D.W., Darbyshire, F., Evans, R.L., Grütter, H., Jones, A.G., and Yuan, X.: The elusive lithosphere–asthenosphere boundary (LAB) beneath cratons, Lithos, 109(1–2), 1–22, 2009.

El-Sharkawy, A., Meier, T., Lebedev, S., Behrmann, J.H., Hamada, M., Cristiano, L., Weidle, Ch., and Köhn. D.: The slab
455   puzzle in the Alpine-Mediterranean Region: Insights from a new, high-resolution, shear wave velocity model of the upper mantle, Geochemistry, Geophysics, Geosystems 21, e2020GC008993, https://doi.org/10.1029/2020GC008993, 2020.

Geissler, W.H., Sodoudi, F. and Kind, R.: Thickness of central and easter European lithosphere as seen by S receiver functions, Geophys. J. Int. 181, 604-634, doi: 10.1111/j.1365-246X.2010.04548.x, 2010.

460   Grad, M., Tira T., and ESC Working Group: The Moho depth map of the European Plate, Geophys. J. Int. 176, 279-292, doi: 10.1111/j.1365-246X.2008.03919.x, 2009a.

Grad, M., Brückl, E., Majdanski, M., Behm, M., Guterch, A., and CELEBRATION 2000 and ALP 2002 Working Groups: Crustal structure of the Eastern Alps and their foreland: seismic model beneath the CEL10/Alp04 profile and tectonic implications, Geophys. J. Int. 177, 279–295, doi: 10.1111/j.1365-246X. 2008.04074.x, 2009b.

465   Guidarelli, M., Aoudia, A., and Costa, G.: 3-D structure of the crust and uppermost mantle at the junction between the Southeastern Alps and External Dinarides from ambient noise tomography, Geophys. J. Int. 211, 1509–1523, doi: 10.1093/gji/ggx379, 2017.

Handy, M. R., Ustaszewski, K., and Kissling, E.: Reconstructing the Alps-Carpathians-Dinarides as a key to understand switches in subduction polarity, slab gaps and surface motion, Int. J. Earth Sci. 104, 1–26. doi: 10.1007/s00531-014-
470   1060-3, 2015.

Handy, M., Schmid, S.M., Paffrath, M. and Friederich, W.: European tectosphere and slabs beneath the greater Alpine area - Interpretation of mantle structure in the Alps-Apennines-Pannonian region from teleseismic Vp studies, Solid Earth, this volume, 2021.

Heit, B., Weber, M., Tilmann, F., Haberland, C., Jia, Y., Carraro, C., and Pesaresi, D.: The SWATH-D Seismic Network in
475   Italy and Austria. GFZ Data Services, https://doi.org/10.14470/mf7562601148, 2017.

Heit, B., Cristiano, L., Haberland, C., Tilmann, F., Pesaresi, D., Jia, Y., Hausmann, H., Hemmleb, S., Haxter, M., Zieke, T., Jäckl, K.-H., Schlömer, A., and Weber, M.: The SWATH-D Seismological Network in the Eastern Alps, Seismol. Res. , Lett. XX, 1–18, https://doi.org/10.1785/0220200377, 2021.

45

Hetényi, G., Ren, Y., Dando, B., Stuart, G.W., Hegedűs, E., Kovács, A.C., and Houseman, G.A.: Crustal structure of the
480   Pannonian Basin: the AlCaPa and Tisza terrains and the Mid-Hungarian Zone, Tectonophysics 646, 106-116,
http://dx.doi.org/10.1016/j.tecto.2015.02.004, 2015.

Hetényi, G., I. Molinari, J. Clinton et al.: The AlpArray Seismic Network: a large-scale European experiment to image the
Alpine orogeny. Surveys in Geophysics, 39, 1009-1033, doi:10.1007/s10712-018-9472-4, 2018a.

Hetényi, G., Plomerová, J., Bianchi, I., Exnerová, H. K., Bokelmann, G., Handy, M. et al.: From mountain summits to roots:
485   crustal structure of the Eastern Alps and Bohemian Massif along longitude 13.3 E, Tectonophysics 744, 239–255, doi:
10.1016/j.tecto.2018.07.001, 2018b.

Horváth, F., Bada, G., Szafian, P., Tari, G., Adam, A. and Cloetingh, S.: Formation and deformation of the Pannonian Basin:
constraints from observational data, Geological Society London Memoirs 32, 191-206,
https://doi.org/10.1144/GSL.MEM.2006.032.01.11, 2006.

490   Horváth, F., Musitz, B., Balázs, A., Végh, A., Uhrin, A., Nádor, A., Koroknai, B., Pap, N., Tóth, T. and Wórum, G.:
Evolution of the Pannonian basin and its geothermal resources. Geothermics, 53, 328–352,
doi.org/10.1016/j.geothermics.2014.07.009, 2015.

Hrubcová, P., Środa, P.,Špicák ,A. , Guterch, A., Grad, M., Keller, G.R., Brueckl, E. and Thybo, H.: Crustal and uppermost
mantle structure of the Bohemian Massif based on CELEBRATION 2000 data, J. Geophys. Res. Solid Earth 110,
495   B11305, doi:10.1029/2004JB003080, 2005.

Kalmár, D., Hetényi, G. and Bondár, I.: Moho depth analysis of the eastern Pannonian Basin and the Southern Carpathians
from receiver functions, J Seismol 23:967–982, https://doi.org/10.1007/s10950-019-09847-w, 2019.

Kästle, E. D., El-Sharkawy, A., Boschi, L., Meier, T., Rosenberg, C., Bellahsen, N. et al.: Surface wave tomography of the
Alps using ambient-noise and earthquake phase velocity measurements. J. Geophys. Res. Solid Earth 123, 1770–1792,
500   doi: 10.1002/2017JB014698, 2018.

Kästle, E. D., Rosenberg, C., Boschi, L., Bellahsen, N., Meier, T., and El-Sharkawy, A.: Slab break-offs in the Alpine
subduction zone, Int. J. Earth Sci. 109, 587–603, doi: 10.1007/s00531-020-01821-z, 2020.

Kennett, B.L.N.. and Engdahl, E.R.: Travel times for global earthquake location and phase identification, Geophys. J. Int.,
105, 429–465, 1991.

505   Kind, R., Handy, M.R., Yuan, X., Meier, T., Kämpf, H. and Somroo, R.: Detection of a new sub-lithospheric discontinuity in
central Europe with S-receiver functions. Tectonophysics, 700–701, 19–31, 2017.

Kind, R., Mooney, W., and Yuan, X.: New insights into structural elements of the upper mantle beneath the contiguous
United States from S-to-P converted seismic phases. Geophys. J. Int., 222, 646–659, doi: 10.1093/gji/ggaa203, 2020.

Kissling, E., Schmid, S. M., Lippitsch, R., Ansorge, J., and Fügenschuh, B.: Lithosphere structure and tectonic evolution of
510   the Alpine arc: new evidence from high- resolution teleseismic tomography, in European Lithosphere Dynamics,
Geological Society Memoirs, London, 32, 29–145, https://doi.org/10.1144/GSL.MEM.2006.032.01.08, 2006.

Kumar, P., Kind, R. , and Yuan, X.: Receiver function summation without deconvolution, Geophys. J. Int., 180(3), 1223–1230. 2010.

Kummerow, J., Kind, R., Oncken, O., Giese, P., Ryberg, T., Wylegalla, K., et al.: A natural and controlled source seismic profile through the Eastern Alps: TRANSALP. Earth Planet. Sci. Lett. 225, 115–129, doi: 10.1016/j.epsl. 2004.05.040, 2004.

Li, X., Yuan, X., and Kind, R.: The lithosphere-asthenosphere boundary beneath the western United States, Geophys. J. Int. 170, 700-710,doi: 10.1111/j.1365-246X.2007.03428.x, 2007.

Lippitsch, R., Kissling, E., and Ansorge, J.: Upper mantle structure beneath the Alpine orogen from high-resolution teleseismic tomography. J. Geophys. Res. Solid Earth 108/B8, 2376. doi: 10.1029/2002JB002016, 2003.

Liu, T., and Shearer, P. M. : Complicated lithospheric structure beneath the contiguous US revealed by teleseismic S-reflections. Journal of Geophysical Research: Solid Earth, 126, e2020JB021624. https://doi. org/10.1029/2020JB021624, 2021.

Lombardi, D., Braunmiller, J., Kissling, E., and Giardini, D.: Moho depth and Poisson's ratio in the Western-Central Alps from receiver functions, Geophys. J. Int., 173(1), 249–264, 2008.

Molinari, I., Verbeke, J., Boschi, L., Kissling, E., and Morelli, A.: Italian and Alpine three-dimensional crustal structure imaged by ambient-noise surface-wave dispersion, Geochem. Geophys. Geosyst., 16, 4405–4421, doi:10.1002/2015GC006176, 2015.

Mroczek, S., Tilmann, F. J., Pleuger, J., Yuan, X., Heit, B., and the AlpArray Working Group: Filling the Moho gap: High resolution crustal structure of the Eastern Alps, T047-04 presented at Fall Meeting, AGU, 1-17 Dec, 2020.

Nabelek, J., Hetényi, G., Vergne, J., Sapkota, S., Kafle, B., Jiang, M., et al.: Underplating in the Himalaya-Tibet collision zone revealed by the Hi-CLIMB experiment. Science, 325(5946), 1371–1374, https://doi.org/10.1126/science.1167719, 2009.

Paffrath, M., Friederich, W., and AlpArray & AlpArray-SWATH D Working Groups: Teleseismic traveltime tomography of the greater Alpine region. Solid Earth, this volume, 2021.

Ratschbacher, L., Frisch, W., and Linzer, H.G.: Lateral extrusion in the Eastern Alps, Part 2: Structural analysis. Tectonics, 10/2, 257-271, 1991.

Spada M., Bianchi I., Kissling E., Agostinetti N.P., and Wiemer S.: Combining controlled-source seismology and receiver function information to derive 3-D Moho topography for Italy, Geophys. J. Int., 194, 1050–1068, 10.1093/gji/ggt148, 2013.

Schmid, S. M., Fügenschuh, B., Kissling, E. and Schuster, R.: Tectonic map and overall architecture of the Alpine orogen. Eclogae Geol. Helv. 97, 93–117, doi: 10.1007/s00015-004-1113-x, 2004.

Schmid, S. M., Bernoulli, D., Fügenschuh, B., Matenco, L., Schefer, S., Schuster, R., Tischler, M., and Ustaszewski, K.: The Alpine-Carpathian-Dinaridic orogenic system: correlation and evolution of tectonic units, Swiss Journal of Geosciences, 101, 139-183, doi: 10.1007/s00015-008-1247-3, 2008.

Schneider, F. M., Yuan, X., Schurr, B., Mechie, J., Sippl, C., Haberland, C., et al.: Seismic imaging of subducting continental lower crust beneath the Pamir, Earth and Planetary Science Letters, 375, 101–112, https://doi.org/10.1016/j.epsl.2013.05.015, 2013

Stammler, K.: Seismic handler programmable multichannel data handler for interactive and automatic processing of seismological analysis, Comput. Geosci., 19 (2), 135-140, 1993.

Szanyi, G., Graczer, Z., Balazsc , B., I.J. Kovacs and AlpArray Working Group: The transition zone between the Eastern Alps and the Pannonian basin imaged by ambient noise tomography, Tectonophysics 805 (228770), https://doi.org/10.1016/j.tecto.2021.228770, 2021.

Wilde-Piórko, M., Saul, J., and Gr, M.: Differences in the crustal and uppermost mantle structure of the bohemian massif from teleseismic receiver functions. Stud Geophys Geod 49:85–107, 2005.

Yan, Q. Z., and Mechie, J.: A fine structural section through the crust and lower lithosphere along the axial region of the Alps, Geophys. J. Int. 98(3), 465–488, 1989.

Yuan, X., Ni, J., Kind, R., Mechie, J., and Sandvol, E.: Lithospheric and upper mantle structure of southern Tibet from a seismological passive source experiment, J. Geophys. Res., 102(B12), 27 491–27 500, 1997.
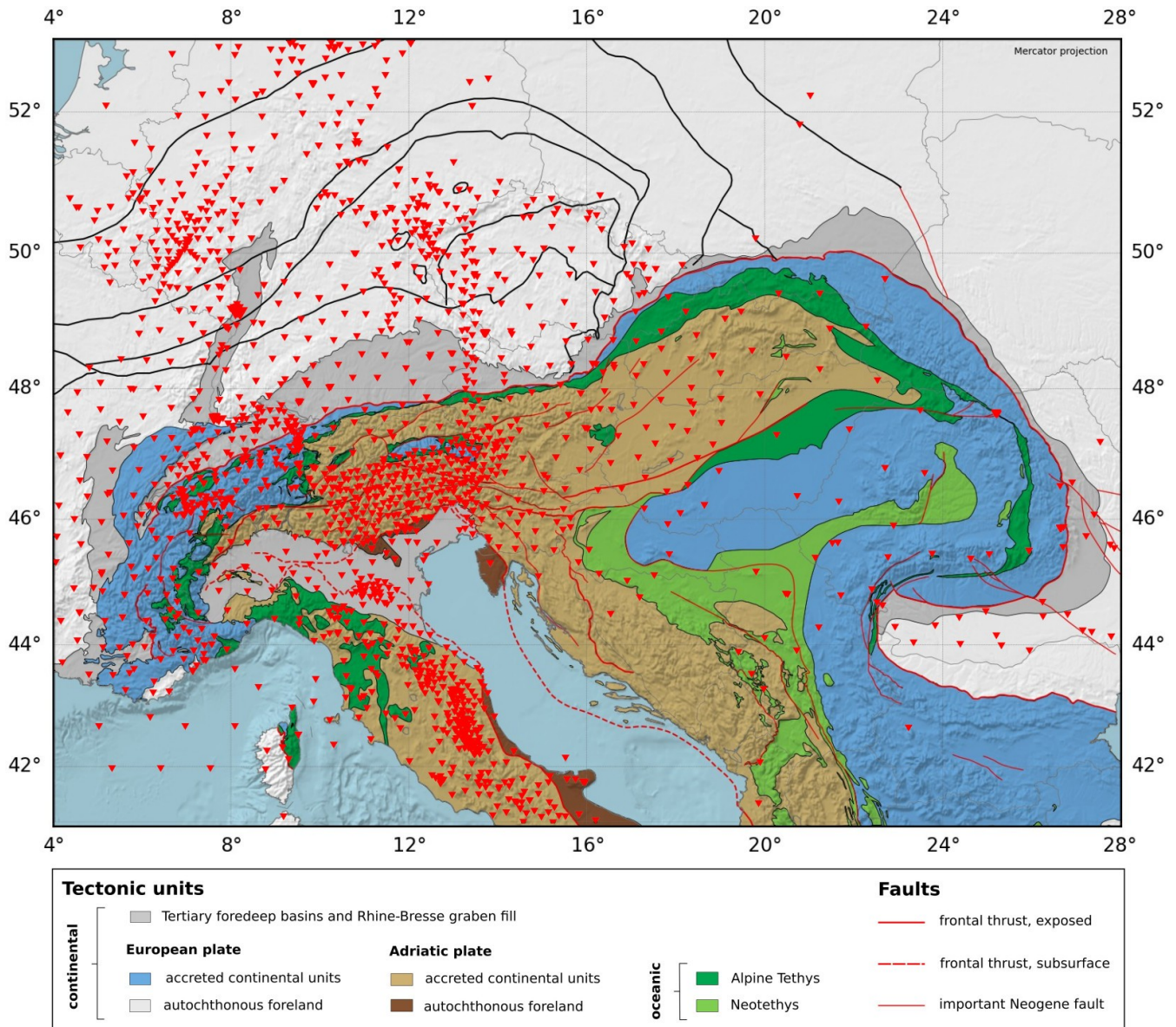
Figure 1: Distribution of permanent and temporary broadband stations used in this study (red inverted triangles) on a geological map of the area (after Hetényi et al. 2018a, their Fig. 1).

565
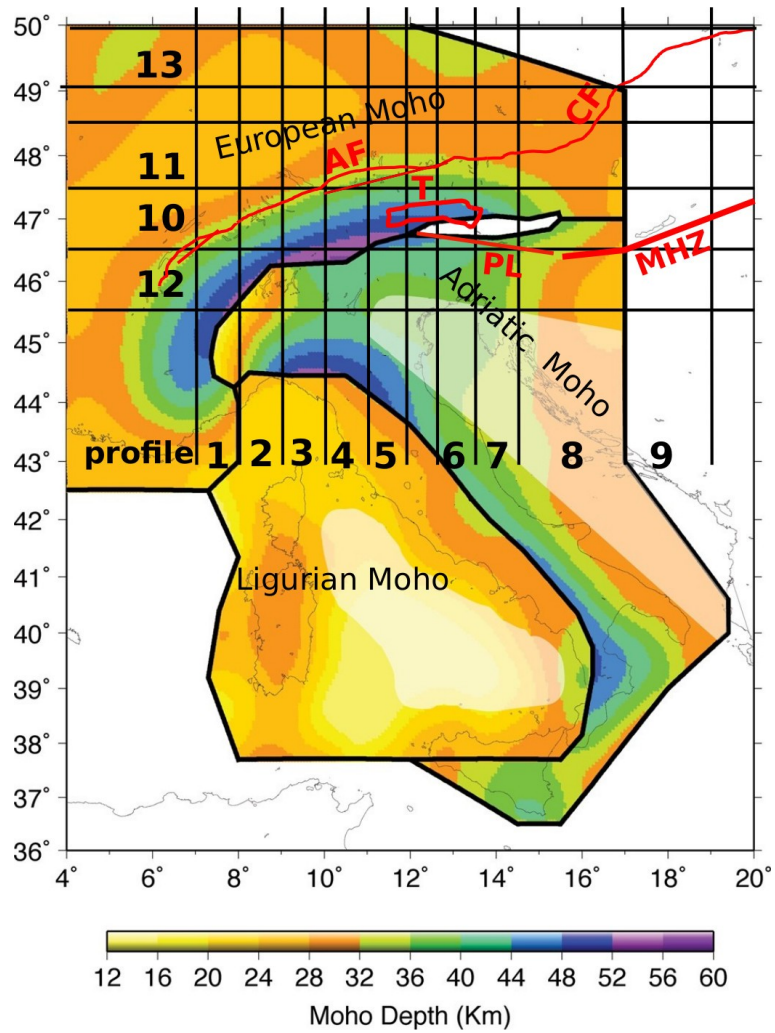
Figure 2: Moho map by Spada et al. (2013) with the locations of the sampling corridors used for profiles 1-13 shown in Fig. 3-14, 20. The locations of the Mid-Hungarian Fault Zone (MHZ) the Periadriatic Line (PL), the Tauern Window (T), the Alpine Front (AF) and the Carpathians Front (CF) are also marked. The space between two black lines marks the width of the profile corridors.

570

575

60
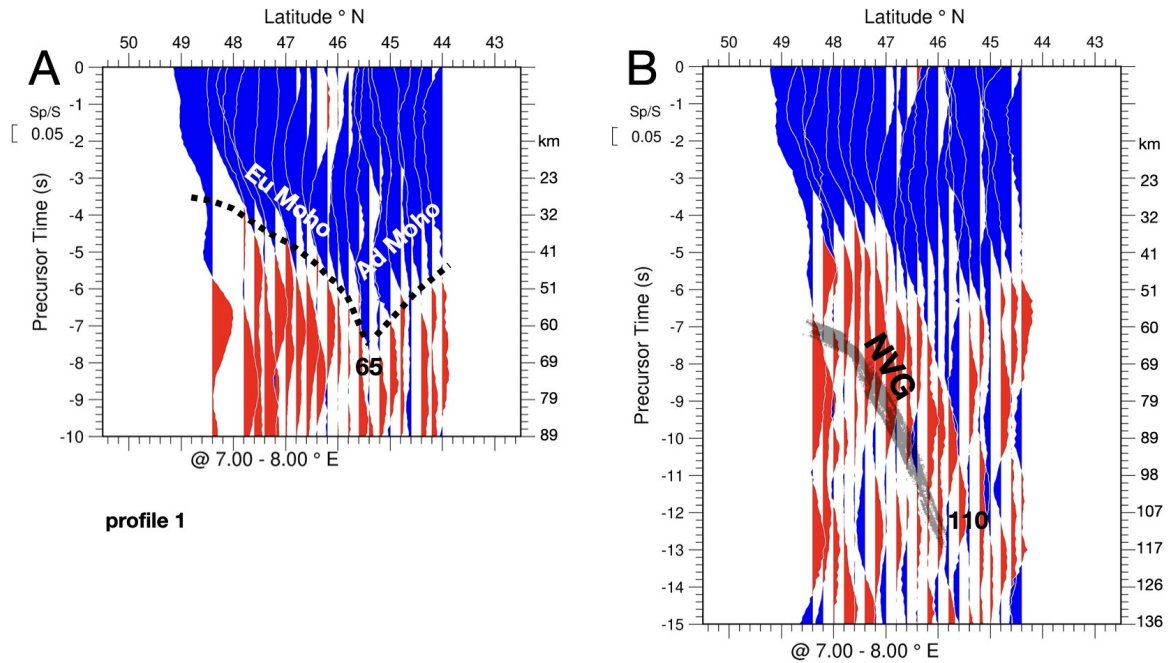
Figure 3: Profile 1: North-south profiles between 7-8°E. Differential times of converted waves relative to the S arrival times are given on the left of sections A and B. These times are converted into depth displayed on the right side of the sections using the global IASP91 velocity model. Blue colors indicate velocity increases with increasing depth (positive amplitudes) and red colors velocity decreases (negative amplitudes), respectively. Note vertical exaggeration of around 8.8 times. A) Section of summation traces within bins of S-to-P piercing points at 50 km depth, appropriate for imaging the Moho. Bin size along the profile is 0.2°, the bin size perpendicular to the profile is given at the bottom of the section. The onsets of the S-to-P converted signals at the Moho are approximated by a black dotted line. "Eu Moho" refers to the European Moho and "Ad Moho" designates the Adriatic Moho, respectively. The number given along the black dotted line in A indicates the greatest depth of the trough formed by the Moho signals. B) Same as in A, but configured for a piercing point depth of 100 km, appropriate for imaging the mantle lithosphere below the Moho. A concentration of negative (red) signals marked NVG (Negative Velocity Gradient) is visible below the Moho. The base of the NVG appears more scattered than the Moho. Therefore, the arrival times are only approximately marked by a scattered grey line. Similarly the number given at the bottom of the NVG in B approximately marks the deepest extend of the NVG. Legends of the following figures with profiles refer to this figure.
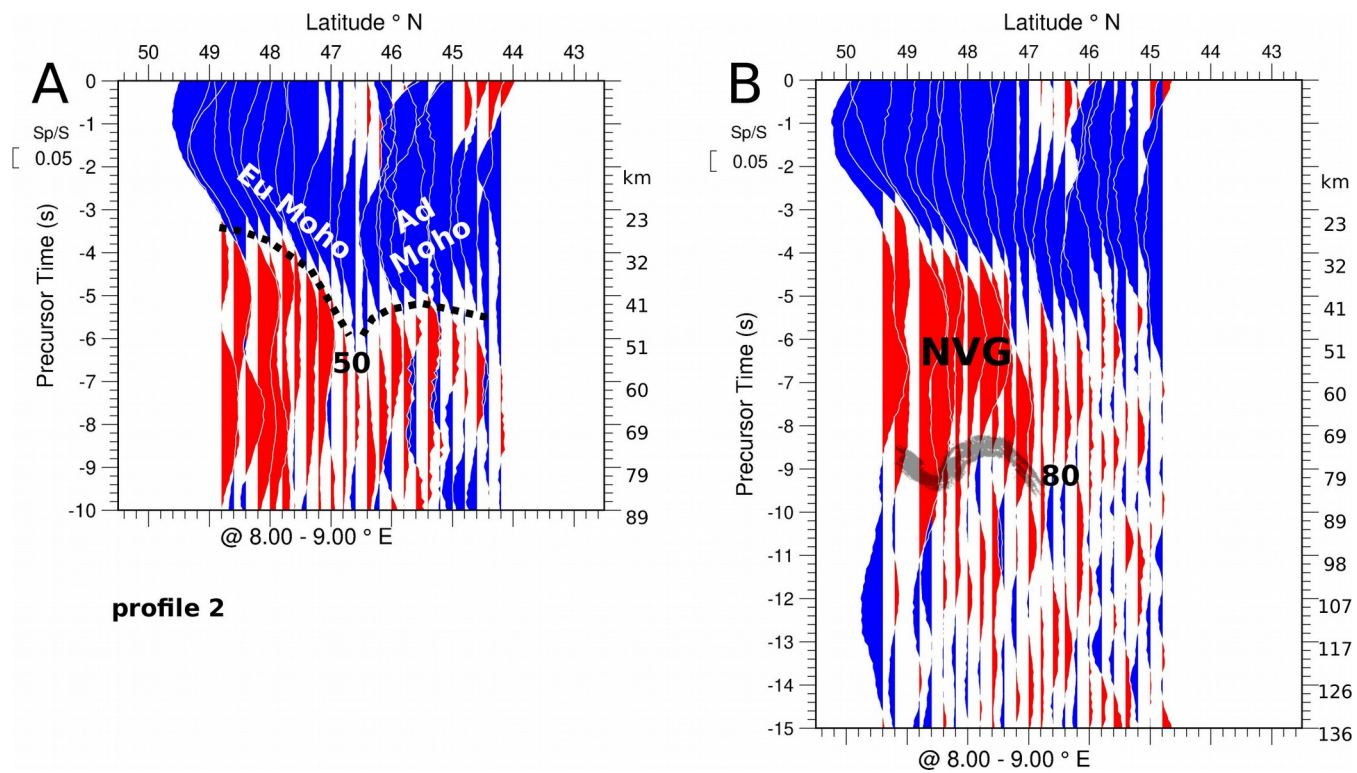
595   **Figure 4:** Profile 2: North-south profiles at 8-9°E. Note that the deepest point of the Moho at 46.5° latitude is slightly north the Europe-Adria boundary at around 46° according to Spada et al. (2013) (see Fig. 2).
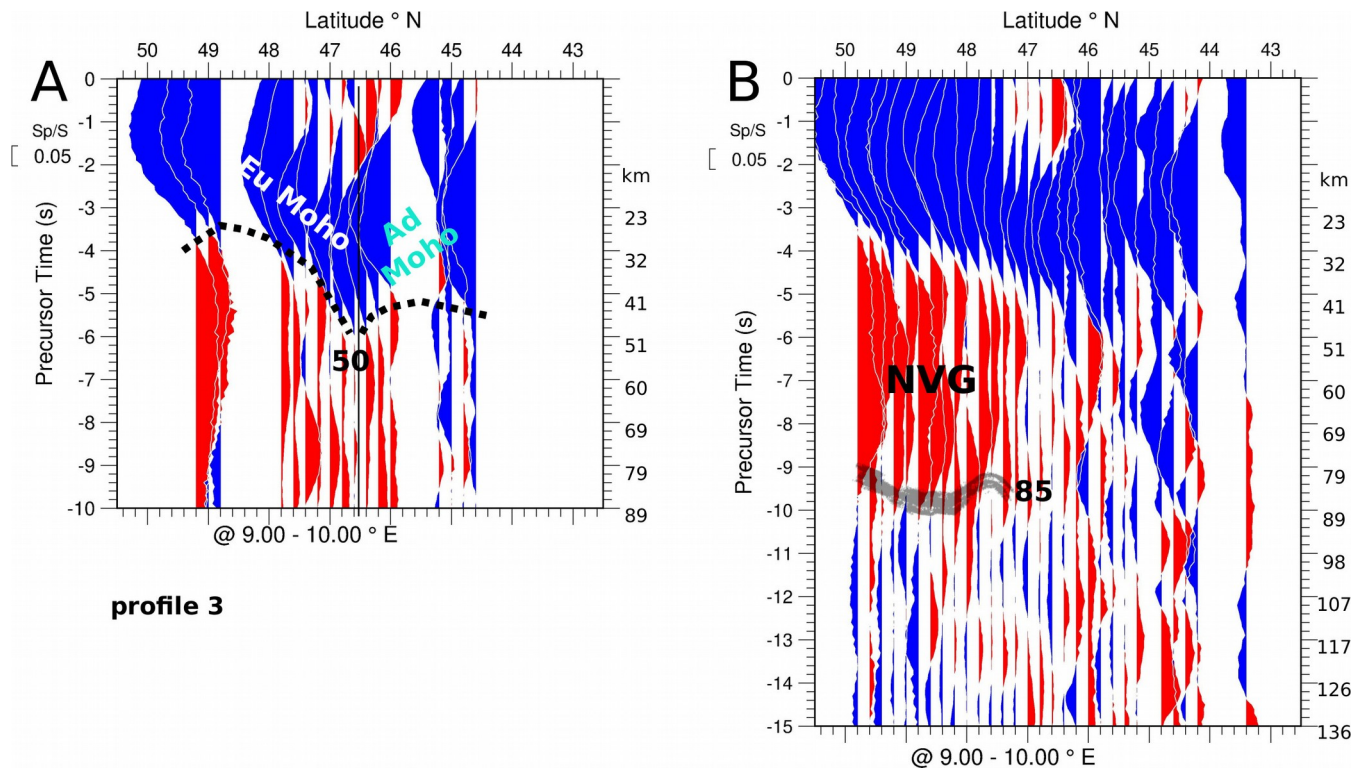
Figure 5: Profile 3: North-south profiles at 9-10°E. Note that the deepest point of the Moho at 46.5° latitude closely coincides with the Europe-Adria boundary according to Spada et al. (2013) (see Fig. 2).

600

605

610

70
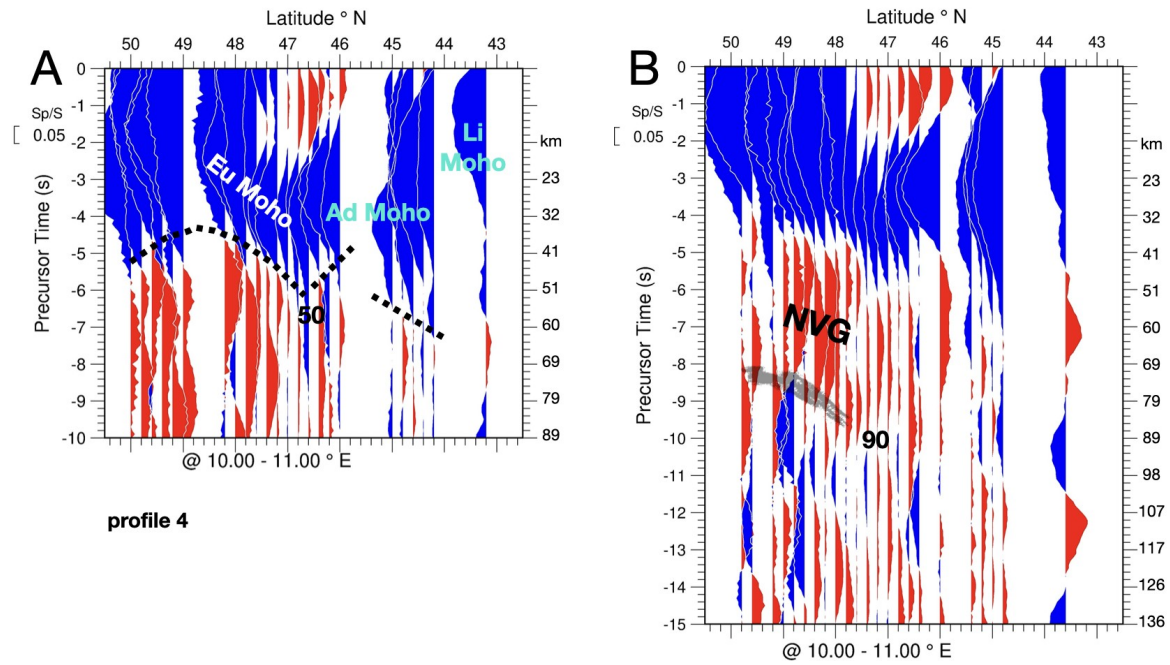
615   **Figure 6:** Profile 4: North-south profiles at 10-11°E. Note that the deepest point of the Moho at 46.5° latitude closely coincides with the Europe-Adria boundary according to Spada et al. (2013) (see Fig. 2). The base of the much shallower Ligurian Moho depicted in Fig. 2 marked "Li Moho" is visible at around 43.5° latitude.

620

625
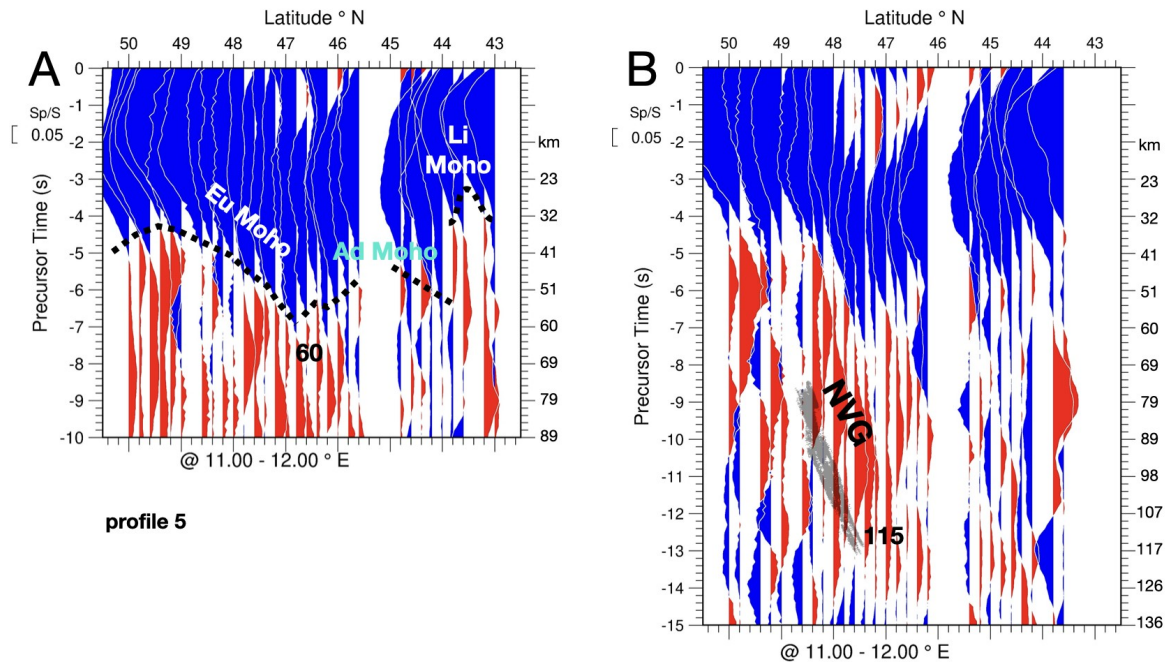
Figure 7: Profile 5: North-south profiles at 11-12°E, i.e. near the western margin of the Tauern Window. Note that the deepest point of the Moho at 46.5° latitude closely coincides with the Europe-Adria boundary according to Spada et al. (2013) (see Fig. 2). The base of the much shallower Ligurian Moho depicted in Fig. 2 marked "Li Moho" is visible at around 43.5° latitude.

75
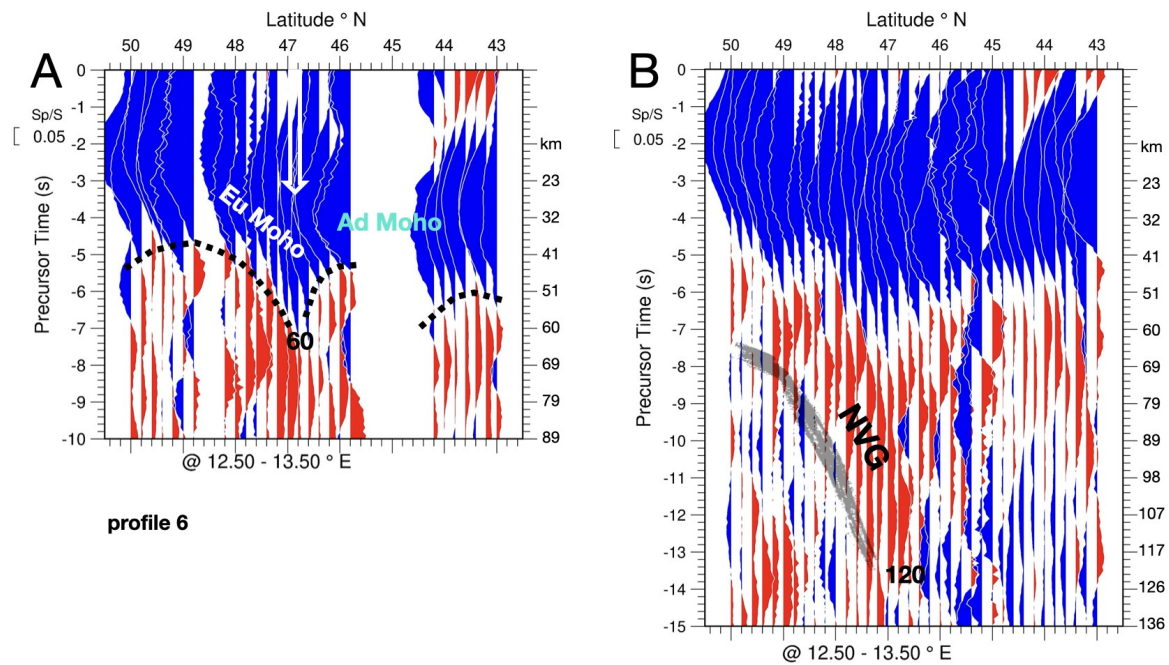
Figure 8: Profile 6: North-south profiles at 12.5-13.5°E, i.e. across the eastern part of the Tauern Window. Note that the deepest point of the Moho near 47° latitude, marked with a white arrow, closely coincides with the Europe-Adria boundary according to Spada et al. (2013) (see Fig. 2). This profile corridor does not reach the Ligurian Moho in the south.
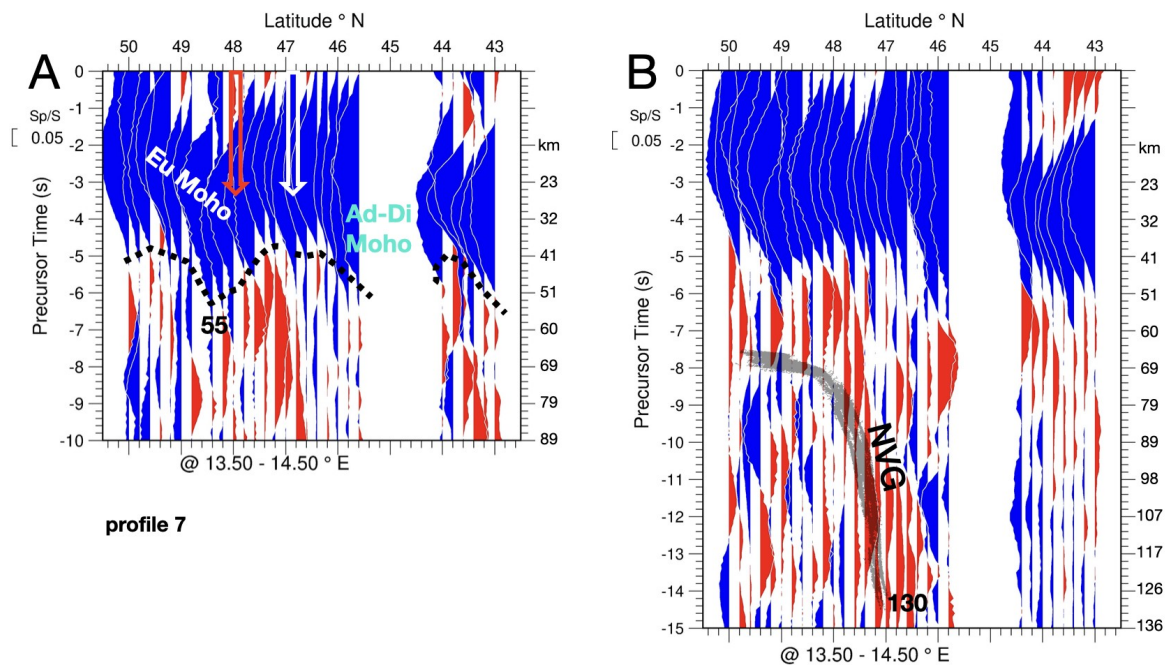
Figure 9: Profile 7: North-south profiles at 13.5-14.5°E, located easterly adjacent to the Tauern Window. "Ad-Di Moho" indicates Adriatic-Dinarides Moho. A) The white arrow locates latitude near 47° indicating where the Moho reached the deepest point in profile 6 of Fig. 8. Note the abrupt along strike change in terms of the Moho topography near 13° E longitude, where this section shows the exact opposite, namely a culmination rather than a through at this same latitude (compare with Fig. 8). This location coincides with the white area in the map of Spada et al. (2013) denoting an area where the Moho is ill constrained by their data. The red arrow indicates the location of the frontal thrust of the Alpine orogen. B) NVG denotes the location of one of the clearest NVG observation in the NS profiles and also in the EW profiles (see Fig. 12B).
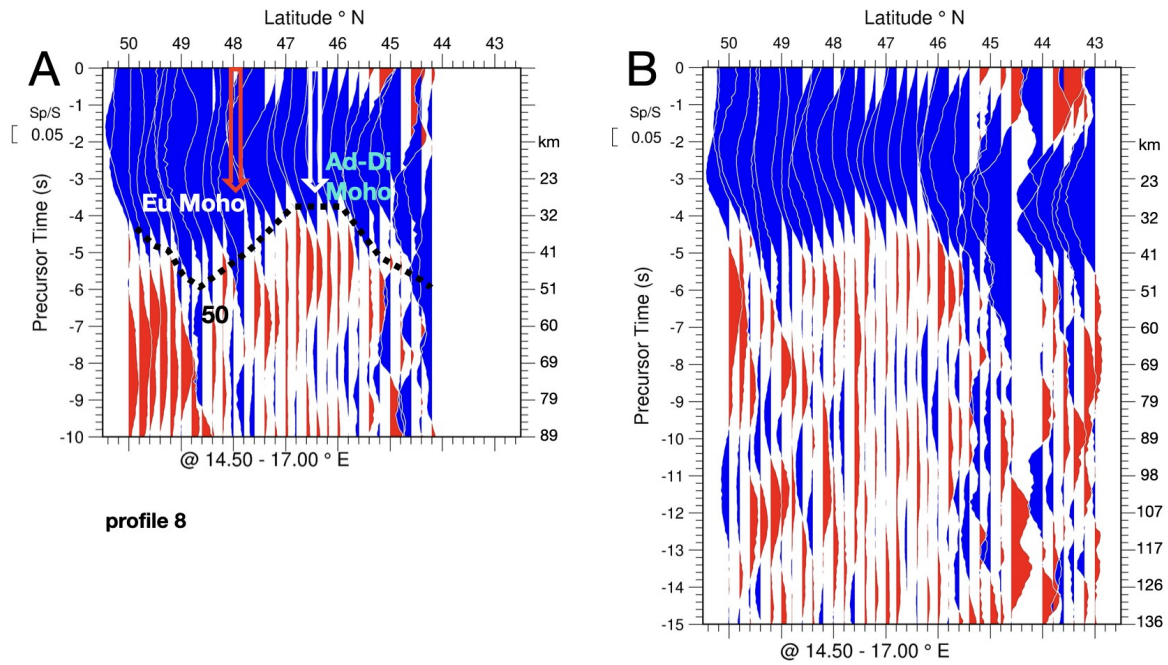
680 **Figure 10:** Profile 8: North-south profiles at 14.5-17°E. As in profile 7 of Fig. 9, the Moho culminates near the junction of European and Adriatic Moho at latitude 46.5° (i.e. at the Mid-Hungarian Fault Zone marked with a white arrow). Ad-Di denotes the Moho beneath the undeformed Adria plate dipping to the NE beneath the Dinarides. The red arrow indicates the location of the frontal thrust of the Alpine orogen.

685

85
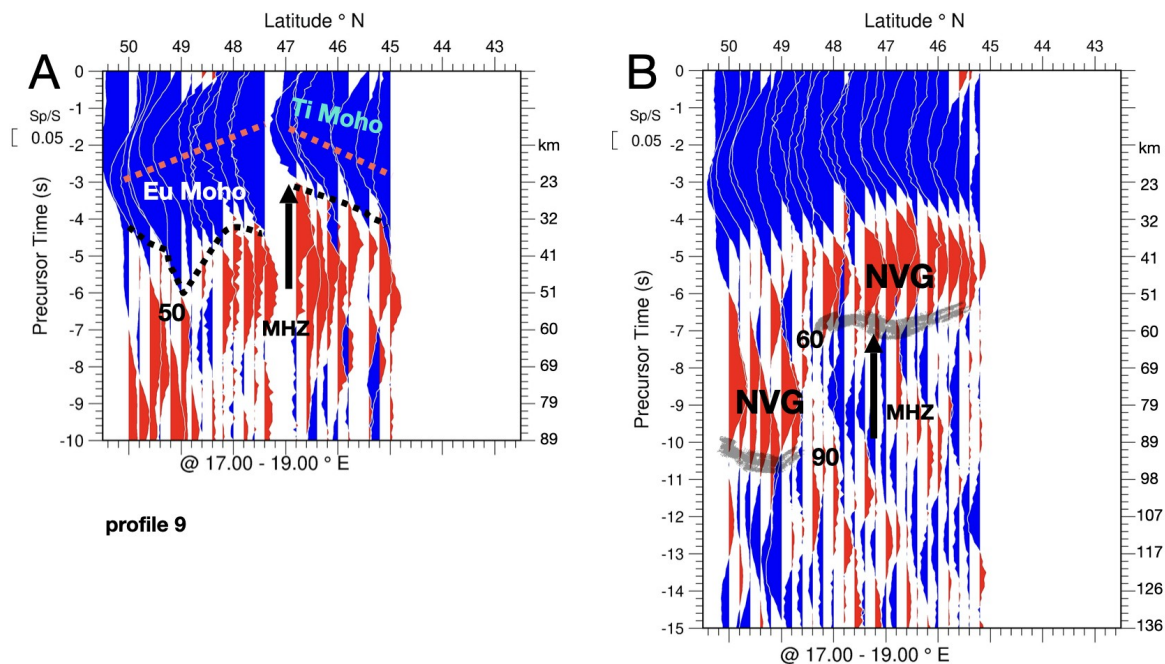
Figure 11: Profile 9:North-south profiles at 17-19°E. As in the profiles 8 of Fig. 10 the Moho culminates in the area of the Mid-Hungarian Fault Zone (MHZ) marked with a black arrow, located in the center of the Pannonian Basin. In this profile the MHZ denotes the boundary of the substantially thinned European crust of the northern part of the Pannonian Basin with the shallow Moho of the southern part of the Pannonian Basin (south of lake Balaton, marked TI Moho) that belongs to the Tisza mega-unit (see Schmid et al. 2008). The red dashed line in Fig. 11A approximately marks the maxima of the Moho waveform.
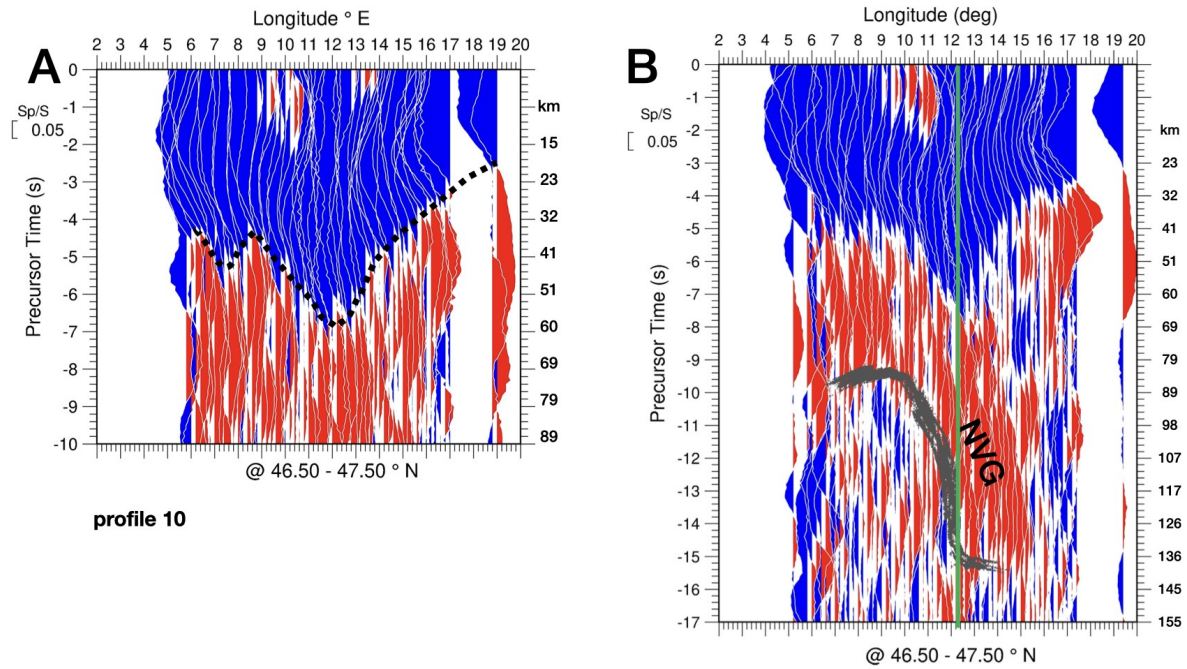
695

Figure 12: Profile 10: East-west profiles at 46.5-47.5°N, largely running within the European plate and straddling the plate boundary east of 11.5°E. Note vertical exaggeration of around 13 times in this E-W profile and those of Fig. 13 and 14. A) Approximate onsets of Moho signals along this profile are marked by a black dotted line. B) Grey shadow indicates the base of the NVG; green vertical line marks a very pronounced along-strike change at around 13°E discussed in the text. B) denotes the clearest observation in the entire area of the steeply dipping NVG.
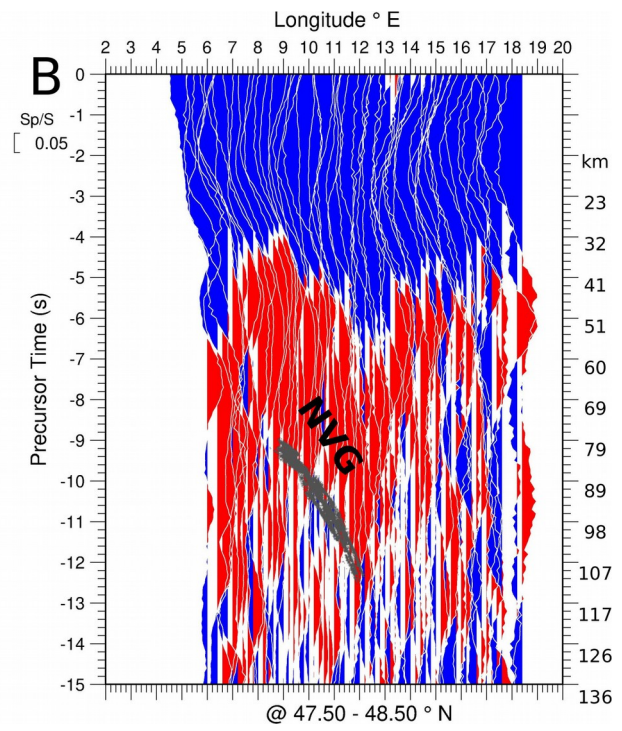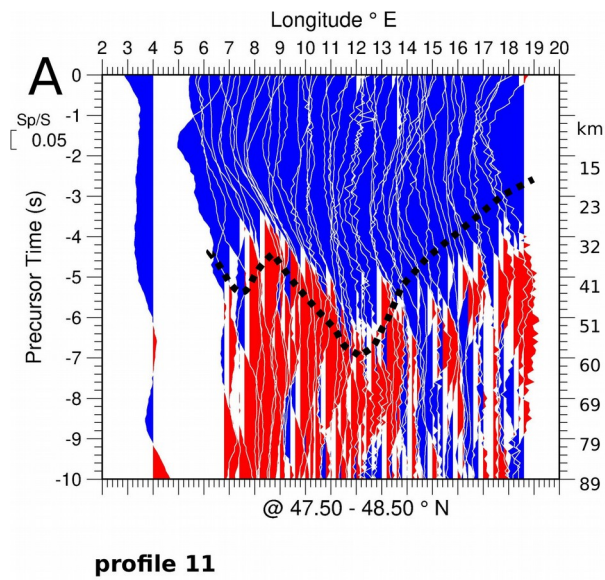
Figure 13: Profile 11: East-west profiles at 47.5-48.5°N running entirely within the European plate. A) The same black dotted line as in profile 10 (Fig. 12) is copied into this figure for comparison.
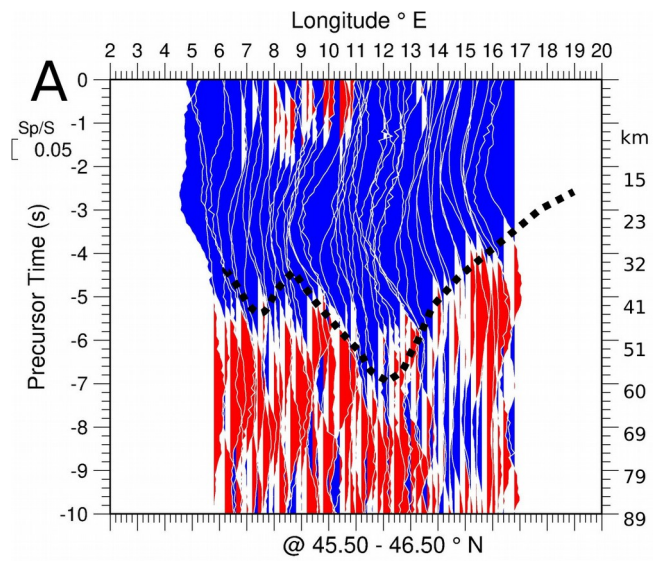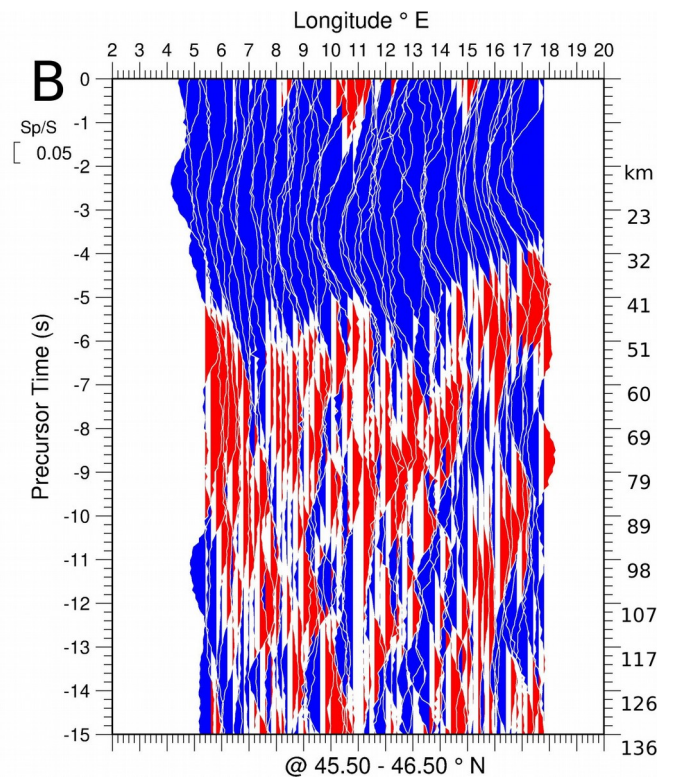
Figure 14: Profile 12: East-west profiles at 45.5-46.5°N, running within the Adriatic plate east of 8°E. A) The same black dotted line as in profile 10 (Fig. 12) is copied into this figure for comparison.
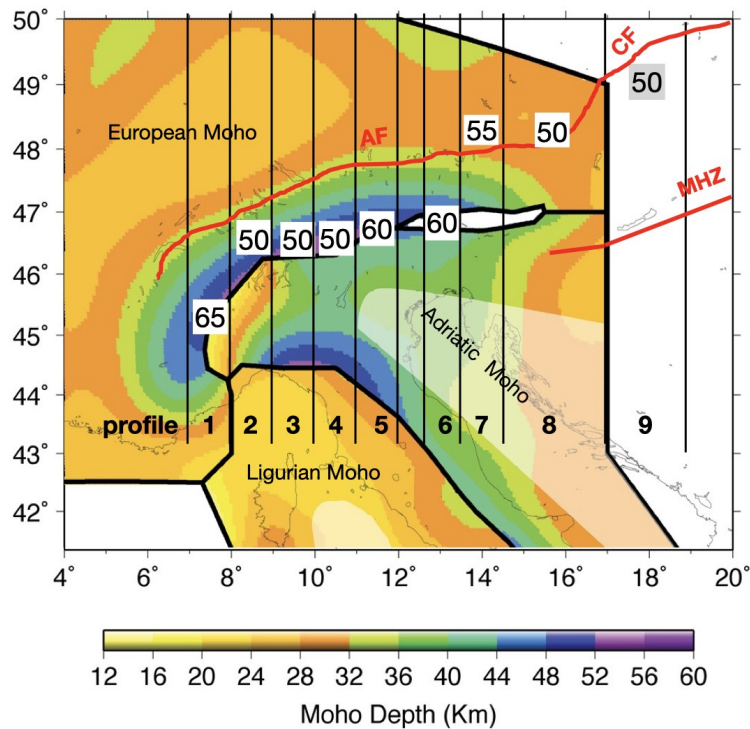
Figure 15: Moho map of Spada et al. (2013) indicating the provisional maximum recorded depths of the Moho along the Alpine chain west of 13.5°E and below the southern part of the Bohemian Massif and below the northernmost West Carpathians, marked in kilometers. These depths are still provisional because we still need to provide do a comparison of the Moho and SV waveforms for more accurate depth determinations in the future. Numbers are taken from profiles 1-12 A. AF, CF and MHZ mark Alpine Front, Carpathian Front and Mid-Hungarian Fault Zone, respectively.
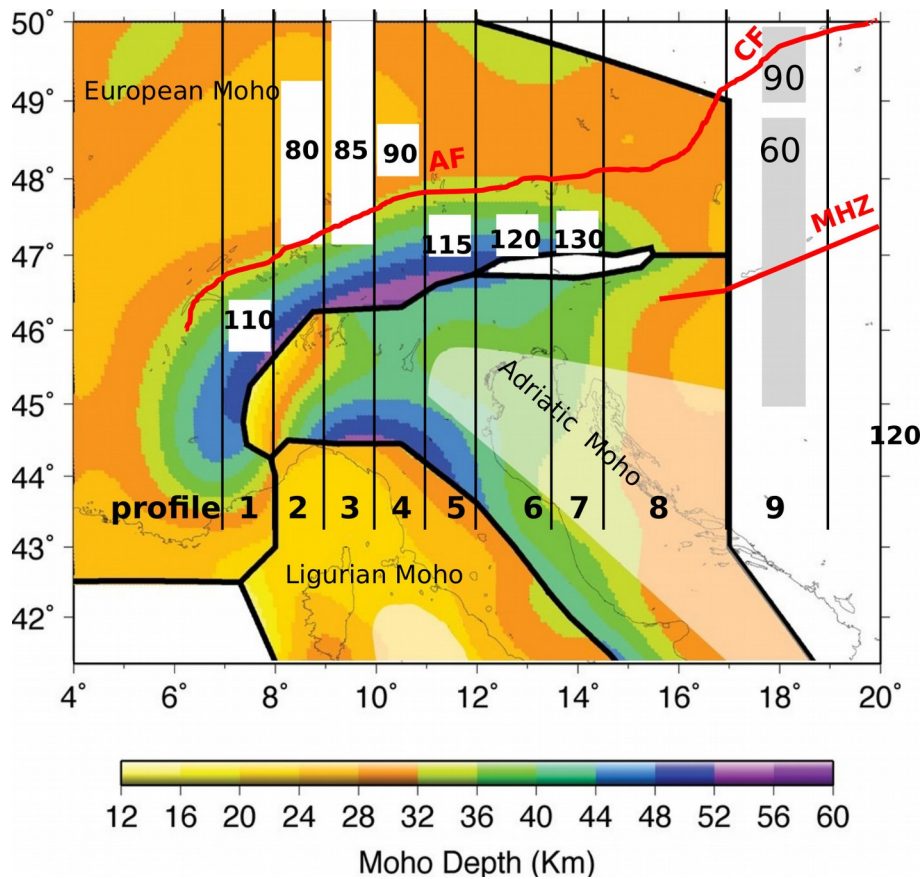
740 **Figure 16:** Moho map of Spada et al. (2013) indicating the provisional maximum recorded depth of the signals at the base of the NVG as marked in profiles 1-12 B. Small white bins in the background of the numbers indicate steeply dipping NVG. Larger backgrounds indicate nearly horizontal NVG.

745

750
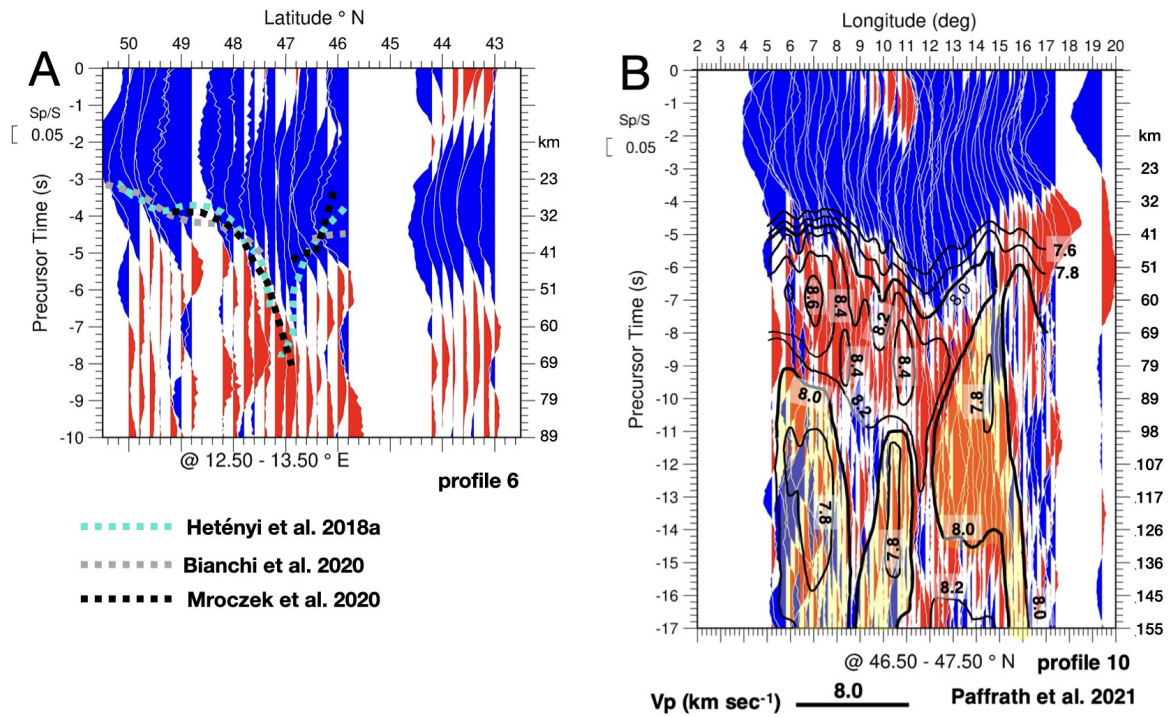
Figure 17: Copies of profiles 6 and 10, superposed with results of earlier studies for comparison. A) Comparison of profile 6, focusing on Moho depth, with profiles of Hetényi et al. (2018b) based on P-receiver functions, Bianchi et al. (2020) based on PKP crustal multiples and Mroczek et al. (2020) also based on P-receiver functions. We did not mark Moho onsets in this figure as in Fig. 8A to allow comparison with the original data without our interpretation. B) Comparison of profile 10, focusing on the depth of the base of the NVG indicated by a grey shadow in Fig. 12B, with absolute P-wave velocities obtained from teleseismic P-wave travel time tomography by Paffrath et al. (2021).
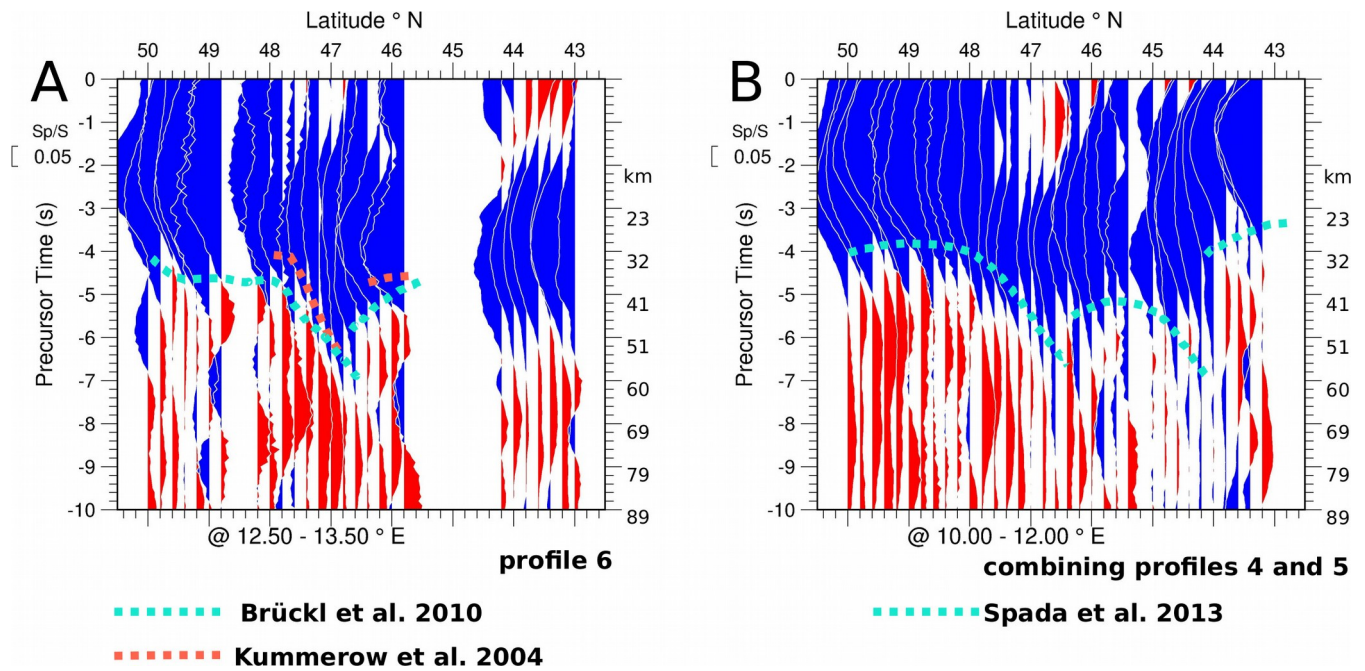
Figure 18: Copies of north-south profiles with results of earlier studies for comparison. A) Comparison of profile 6 (Fig. 8A) with Brückl et al. (2010; their Fig. 3a), who used Moho data of Behm et al. (2007) based on wide-angle reflection and refraction data, and, with Kummerow et al. (2004) using the P-receiver function method. B) Comparison of a combination of the corridors of profiles 4 and 5 (Figs.6A and 7A) with the same profile taken from map of Spada et al. (2013).
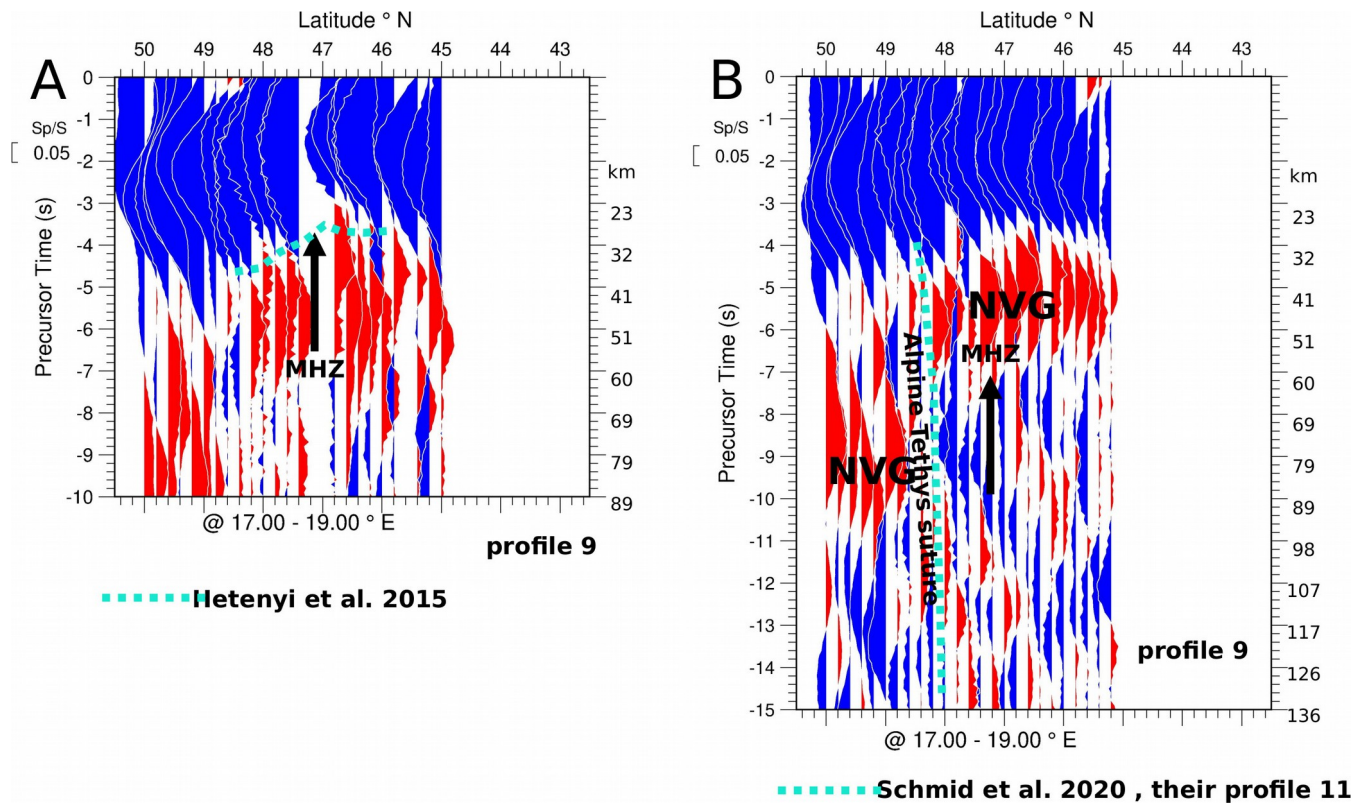
Figure 19: A) Copy of profile 9 (Fig. 11A) across the MHZ superimposed with a study by Hetényi et al. (2015) who used P-receiver functions. B) Copy of profile 9 (Fig. 11B) superimposed with the location of the Alpine Tethys suture as interpreted by Handy et al. (2021) based on mantle tomography by Paffrath et al. (2021).
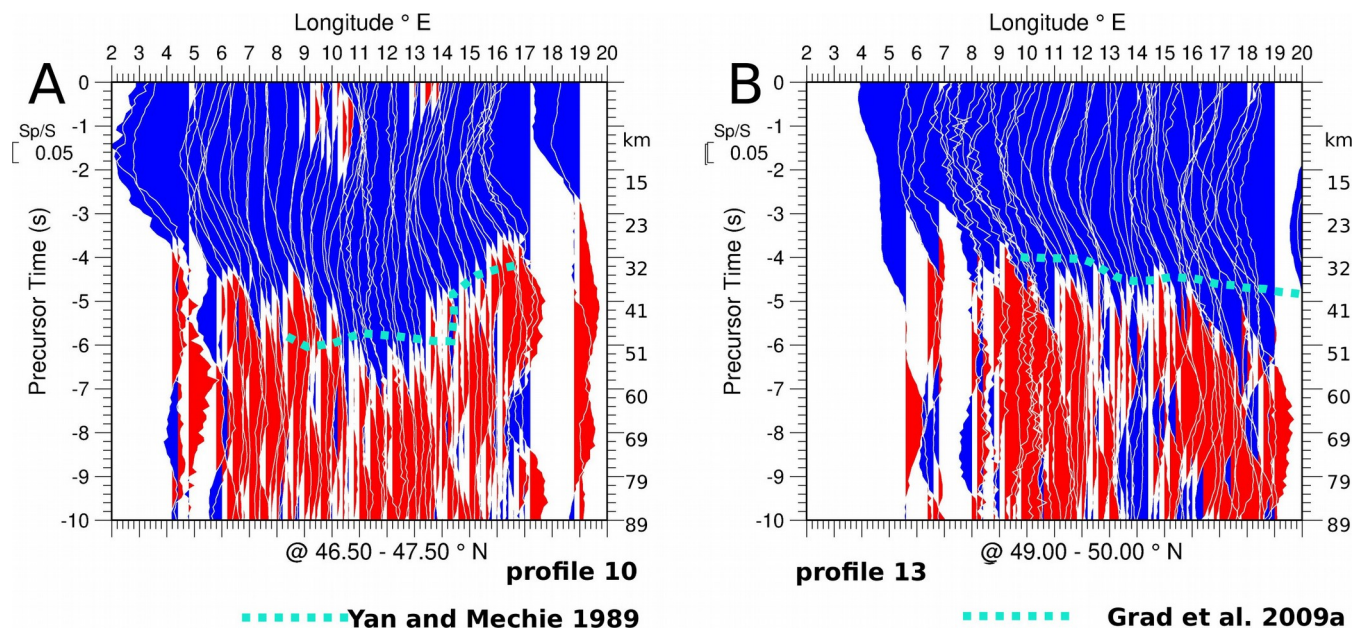
Figure 20: A) Copy of profile 10 (Fig. 12A) with results of Yan and Mechie (1989) who used data from a refraction profile along the Alpine chain. B) Additional east-west profile well north of the earlier profiles shown, constructed for comparison with the Moho map of Grad et al. (2009a) and comparison with profile 10 of Fig. 20A. Note the substantial difference in Moho depth between our data east of 14°E and those of Grad et al. (2009a). Also note that we see pronounced Moho deepening towards the east in this northerly located profile located in the European lithosphere, which contrasts with Moho shallowing towards the east in the southern profile of Fig. 20A located in the Pannonian region (see Fig. 2 for location of the profiles).